nature communications

Article

https://doi.org/10.1038/s41467-024-53135-2

Intermetallics triggering pyroptosis and disulfidptosis in cancer cells promote anti-tumor immunity

Received: 12 May 2024

Accepted: 3 October 2024

Published online: 08 October 2024

Check for updates

Yanlin Zhu[1], Xinxin Wang[2], Lili Feng[1] ✉, Ruoxi Zhao[1], Can Yu[2], Yuanli Liu[3], Ying Xie[4], Bin Liu[1], Yang Zhou[2] ✉ & Piaoping Yang[1] ✉

Pyroptosis, an immunogenic programmed cell death, could efficiently activate tumor immunogenicity and reprogram immunosuppressive microenvironment for boosting cancer immunotherapy. However, the overexpression of SLC7A11 promotes glutathione biosynthesis for maintaining redox balance and countering pyroptosis. Herein, we develop intermetallics modified with glucose oxidase (GOx) and soybean phospholipid (SP) as pyroptosis promoters (Pd_2Sn@GOx-SP), that not only induce pyroptosis by cascade biocatalysis for remodeling tumor microenvironment and facilitating tumor cell immunogenicity, but also trigger disulfidptosis mediated by cystine accumulation to further promote tumor pyroptosis in female mice. Experiments and density functional theory calculations show that Pd_2Sn nanorods with an intermediate size exhibit stronger photothermal and enzyme catalytic activity compared with the other three morphologies investigated. The peroxidase-mimic and oxidase-mimic activities of Pd_2Sn cause potent reactive oxygen species (ROS) storms for triggering pyroptosis, which could be self-reinforced by photothermal effect, hydrogen peroxide supply accompanied by glycometabolism, and oxygen production from catalase-mimic activity of Pd_2Sn. Moreover, the increase of $NADP^+$/NADPH ratio induced by glucose starvation could pose excessive cystine accumulation and inhibit glutathione synthesis, which could cause disulfidptosis and further augment ROS-mediated pyroptosis, respectively. This two-pronged treatment strategy could represent an alternative therapeutic approach to expand anti-tumor immunotherapy.

Cancer is one of the leading causes of death worldwide and exhibits an increasing shift from elderly to middle-aged individuals, in which colorectal cancer is predominant among adults younger than 50 years[1–3]. Owing to the metabolic reprogramming and genetic mutation, cancer cells usually possess elevated oxidative stress characteristics compared with those of nonmalignant cells[4–6]. To pose the excessive production of reactive oxygen species (ROS) is detrimental to cancer cells, which has been confirmed as an efficacious cancer therapy. While cancer cells tend to maintain sufficient glutathione (GSH) levels to neutralize ROS for achieving cell survival and proliferation[7]. Therefore,

[1]Key Laboratory of Superlight Materials and Surface Technology, Ministry of Education, College of Materials Science and Chemical Engineering, Harbin Engineering University, Harbin, PR China. [2]Department of Radiology, Harbin Medical University Cancer Hospital, Harbin, PR China. [3]Department of Biochemistry and Molecular Biology, Harbin Medical University, Harbin, PR China. [4]Key Laboratory of Functional Inorganic Material Chemistry, Ministry of Education, School of Chemistry and Materials Science, Heilongjiang University, Harbin, PR China. ✉e-mail: fenglili@hrbeu.edu.cn; zhouyang094@126.com; yangpiaoping@hrbeu.edu.cn

blocking the synthesis of GSH is expected to achieve maximum cancer cell death. Cysteine is a crucial amino acid that affords the rate-limiting precursor for the biosynthesis of GSH[8,9]. In general, the overexpressed solute carrier family 7 member 11 (SLC7A11) in most cancer cells could import extracellular cystine (an oxidized cysteine dimer), which could be reduced into cysteine in the cytoplasm with the assistance of glucose-derived nicotinamide adenine phosphate (NADPH). The cysteine could serve as a precursor for the subsequent synthesis of GSH to achieve antioxidant defense[8,10]. Thus, the inhibition of NADPH supply could trigger the accumulation of cystine, thereby leading to the reduction of GSH[10]. Meanwhile, the overloading of cystine could endow actin cytoskeleton proteins with abundant disulfides and disulfide bonds, resulting in disulfidptosis caused by disulfide stress[6,11].

Besides the suppression of GSH, promoting massive ROS production also plays a critical role in intensive tumor treatments. The slightly acid and overexpressed hydrogen peroxide (H_2O_2) of tumor microenvironment (TME) create excellent conditions for the production of ROS catalyzed by nanocatalysts[12]. Intermetallics composed of two or more metallic elements display expanded and superior catalytic activity owing to the tuned electronic states and the synergistic effect between the two metals[13,14]. Significantly, the positions of all atoms in intermetallics are assigned with specific sites, leading to the defined stoichiometry and crystal structure[15]. Compared with common alloys with occupy random sites, the regular structure endows the intermetallics with homogeneity of the active sites, which could ensure the abundant generation of ROS[16]. In addition to the enhancement of catalytic activity, the stability of intermetallics could also be improved, which makes them perform better in various physiological environments. This enhancement could be attributed to the mixed bonding, which leads to a more negative free energy of formation than random alloys[17]. Besides the ordered structure, the shape of intermetallics has an influence on the crystal plane and active sites, which could also determine the catalyst performance[18]. Thus, developing well-controlled intermetallics with tuned size and shape is attractive in improving the catalytic capacity and optimizing the formation of ROS for effective cancer therapeutics.

Furthermore, previous research has validated the decisive role of ROS in inducing immunogenic programmed cell death, which could efficiently arouse acute inflammatory response and trigger robust antitumor immune activity[19–21]. Characterized by the activation of Caspase-1 and cleavage of gasdermin D (GSDMD), pyroptosis is an inflammatory cell death. The N-terminal domain of GSDMD (N-GSDMD) could perforate the plasma membrane and induce cell membrane rupture, releasing the bountiful pro-inflammatory cytokine and tumor antigens, which could provoke precision cancer immunotherapy[22–24]. Delightedly, a low level of pyroptosis (<15%) in tumor cells could achieve an efficacious anti-tumor immunity[25]. Consequently, the ROS-induced pyroptosis could not only kill cancer cells by cell membrane perforation, but also facilitate the initiation and infiltration of T cells owing to the release of cytoplasmic contents, which could remodel the tumor immunosuppressive microenvironment and transform cold tumor (immune-indolent noninflamed tumor phenotype) into hot tumors (inflammatory phenotype)[24,26]. Therefore, exploring the effective strategies to amplify oxidative stress-triggered pyroptosis while synchronously magnifying immunity responses in the TME offers a distinctive direction for cancer therapy.

In this work, we report the intermetallics modified with glucose oxidase (GOx) and soybean phospholipid (SP) as nano-inducers (Pd_2Sn@GOx-SP) to elicit potent anti-tumor immune responses by pyroptosis and disulfidptosis (Fig. 1). To begin with, the Pd_2Sn intermetallics with different morphologies are developed and their performance are contrasted both in experiments and density functional theory (DFT) calculations. Among them, the Pd_2Sn nanorods (NRs) with the largest specific surface area exhibit the optimal photothermal and enzyme catalytic activities, including peroxidase (POD)-mimic and catalase (CAT)-mimic catalytic activity. In addition, the modification of GOx on the Pd_2Sn intermetallics could serve as a triple role: (1) degrade glucose to afford H_2O_2 for the cascade catalysis reaction, triggering a strong ROS storm; (2) reduce GSH synthesis to defeat the antioxidant defense mechanism of cells and aggravate oxidative stress; (3) inhibit NADPH supply by regulating the glycometabolism to induce the accumulation of cystine, resulting in disulfidptosis. Moreover, the CAT-mimic catalytic activity of Pd_2Sn intermetallics could effectively restore the O_2 levels and further enhance the breakdown of glucose, thereby achieving a self-promoted process. This potent and persistent cellular oxidative pressure could effectively activate and amplify ROS-mediated pyroptosis. In summary, the integration of Pd_2Sn intermetallics and GOx could arouse self-reinforced ROS storm and glucose consumption, which could cause Caspase-1-dependent pyroptosis and cystine-mediated disulfidptosis, leading to the reprogramming of immune microenvironment. Meanwhile, the change of immunosuppressive microenvironment, including the ameliorative infiltration of T cells ($CD4^+$ and $CD8^+$) and M1-like phenotype repolarization of macrophages, could achieve efficacious immunotherapy by activating immune response, counteracting tumor recurrence and metastasis.

Results

Construction and characterization of Pd_2Sn@GOx-SP nanocomposites

The intermetallic compounds of Pd_2Sn nanoparticles with different morphologies were synthesized through one step by the co-reduction of palladium(II) acetylacetonate [$Pd(acac)_2$] and tin(II) acetate [$Sn(OAc)_2$], as shown in Fig. 1a. Methylamine hydrochloride (MAHC) played an important role in controlling the morphology of Pd_2Sn intermetallics, including nanodots (NDs, without MAHC) and NRs in different sizes (with different amounts of MAHC). The representative transmission electron microscopy (TEM) micrographs and elemental mapping of the Pd_2Sn intermetallics were shown in Fig. 2a, b and Supplementary Fig. 2a–c, respectively. The Pd_2Sn intermetallics exhibited the uniform controllable morphology of NRs and NDs, as well as the homogeneous distribution of corresponding elements, confirming the successful construction of intermetallics with different morphologies. High-resolution TEM (HRTEM) of the Pd_2Sn intermetallics revealed the interfacial lattice spacings of 0.195 nm (NRs) and 0.236 nm (NDs), which could be identified as (3 2 0) and (0 2 1) crystal planes of the orthorhombic phase, respectively (Fig. 2c, d and Supplementary Fig. 2d, e). In addition, the coexistence of Pd and Sn elements (with a ratio of 2:1) could also be observed from the energy-dispersive spectroscopy (EDS) spectrum (Fig. 2e), suggesting the successful synthesis of Pd_2Sn intermetallics. Powder X-ray diffraction (PXRD) patterns of Pd_2Sn intermetallics were presented in Fig. 2f and Supplementary Fig. 2, the diffraction peaks showed good crystallinity with the lattice parameter of $a = 8.11$ Å, $b = 5.662$ Å, $c = 4.234$ Å, which matched well with the pure orthorhombic Pd_2Sn phase (PDF 00-026-1297). The Pd_2Sn with two inequivalent Pd sites is cotunnite structured and crystallizes in the orthorhombic Pnma space group (Fig. 2g).

Additionally, X-ray photoelectron spectroscopy (XPS) was performed to analyze the composition and valence state information of Pd_2Sn intermetallics (NDs and NRs). The as-prepared Pd_2Sn intermetallics were mainly composed of Pd, Sn, and O elements (Fig. 2h). The Pd 3*d* region of Pd_2Sn intermetallics in the high-resolution XPS spectrum could be assigned to the spin-splitting orbits of $3d_{3/2}$ and $3d_{5/2}$, and the binding energies at 341.0 and 335.9 eV were attributed to Pd^{2+}, while the peaks at 340.1 and 335.0 eV were assigned to Pd^0 (Fig. 2i). This result confirmed the coexistence of Pd^0 (77%) and Pd^{2+} (23%) in Pd_2Sn NRs and Pd^0 (74%) and Pd^{2+} (26%) in Pd_2Sn NDs. Meanwhile, the high-resolution XPS spectrum for Sn 3*d* of Pd_2Sn intermetallics exhibited a distinct decomposition, verifying the existence of tin with two distinct valence states (Fig. 2j). The characteristic peaks at 486.6 eV ($3d_{5/2}$) and 497.4 eV ($3d_{3/2}$) were attributed to Sn^{4+},

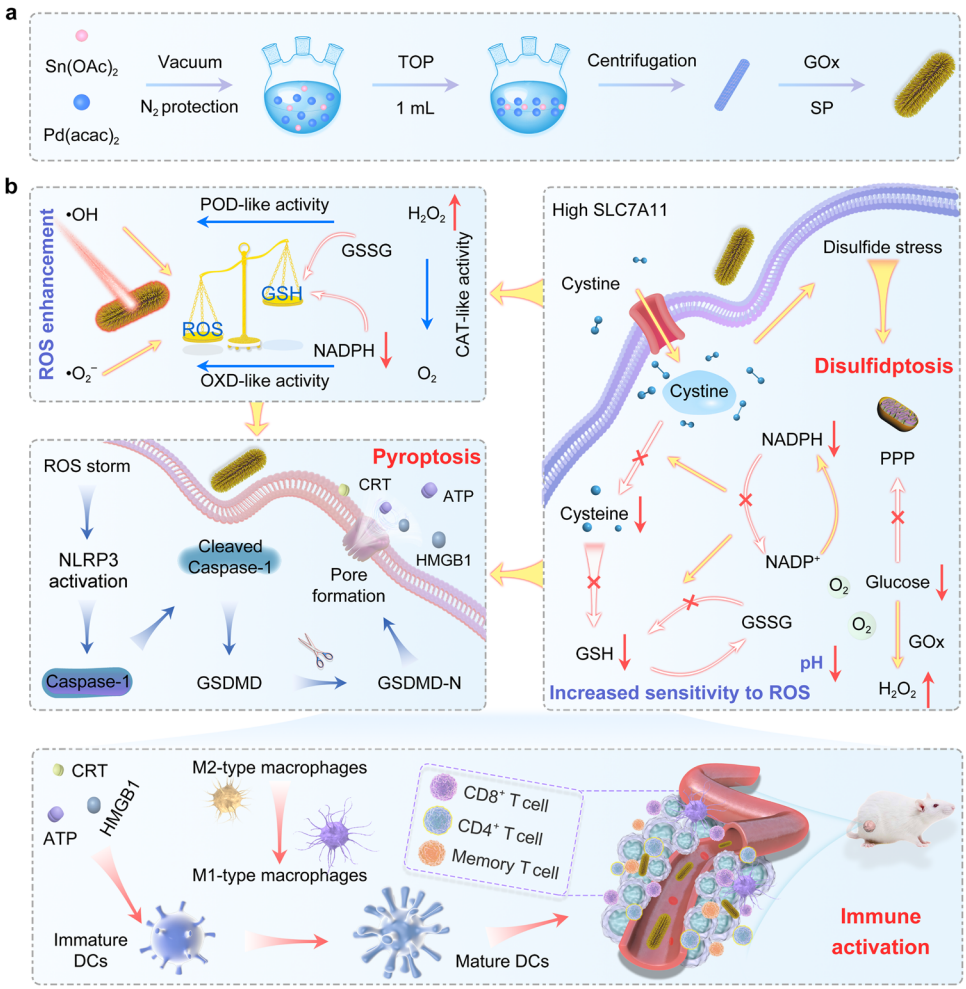

Fig. 1 | Schematic illustration of nanocomposites synthesis and synergistic therapy process. a Schematic diagram of the construction of Pd_2Sn@GOx-SP. **b** Anti-cancer mechanism of synergistic immunity activation induced by Pd_2Sn@GOx-SP by pyroptosis and disulfidptosis.

while the peaks at 486.0 eV ($3d_{5/2}$) and 496.7 eV ($3d_{3/2}$) were associated with Sn^{2+}, and the component at 484.5 eV ($3d_{5/2}$) and 494.8 eV ($3d_{3/2}$) corresponded to metallic Sn. Furthermore, we also investigated the change of elements in the valence state after prolonged oxidation (Supplementary Fig. 3a, b). The majority of the surface Sn was in the oxidized state and the surface Pd was mainly in the metallic state, indicating the surface Sn atoms are more easily oxidized than Pd atoms. These results validated that the Pd_2Sn intermetallics could generate more ROS through the redox reaction[27]. The corresponding elemental mapping, EDS spectrum, and Fourier transform infrared spectrum (FT-IR) showed that the surface of Pd_2Sn intermetallics interacted with Tri-n-octylphosphine (TOP) due to the coordination potence of phosphine ligands (Supplementary Figs. 4 and 5a). To endow the Pd_2Sn intermetallics with high biocompatibility, the SP was further functionalized on the surface of Pd_2Sn intermetallics to obtain Pd_2Sn-SP nanocomposites[28]. Significantly, the surface of Pd_2Sn intermetallics was further modified with GOx, which could facilitate the cascade catalytic reaction to generate more ROS by the enhancement of H_2O_2 catalyzed by GOx. The successful functionalization of SP and modification of GOx were confirmed by the FT-IR spectrum (Supplementary Fig. 5b). Thermogravimetric analysis (TGA) confirmed that the proportion of SP on Pd_2Sn-SP nanocomposites was ~20.81% (Supplementary Fig. 6). In addition, the zeta potentials showed obvious changes from 0.13 to −29.93 mV after the functionalization of SP, and the zeta potential of Pd_2Sn@GOx-SP was further changed to −23.0 mV (Supplementary Fig. 7a). Furthermore, the hydrodynamic size of Pd_2Sn@GOx-SP nanocomposites in phosphate buffer saline (PBS) was ~90 nm according to the analysis of dynamic light scattering, and the average size of Pd_2Sn@GOx-SP at various solvents was also evaluated (Supplementary Fig. 7b). The Pd_2Sn@GOx-SP exhibited a uniform hydrated particle size over 7 days, demonstrating the ideal stability of Pd_2Sn@GOx-SP in physiological conditions, which is a prerequisite for better subsequent application.

Photothermal and multi-enzymatic catalytic activity evaluation

As a noble metal, palladium exhibits the peculiar localized surface plasmon resonance (LSPR) effect and various enzyme catalytic activity, which has made a profound study (Fig. 3a)[29–32]. To begin with, the optical properties of Pd_2Sn-SP nanocomposites (NDs and NRs) were explored by using UV–vis–NIR absorbance spectrum (Fig. 3b and Supplementary Fig. 8), the adsorption intensity of Pd_2Sn-SP NDs and NRs increased linearly with an elevation of concentration. Especially, the Pd_2Sn-SP NRs exhibited stronger absorption (5.33 L g^{-1} cm^{-1}) than Pd_2Sn-SP NDs with the extinction coefficient was 2.30 L g^{-1} cm^{-1}. Subsequently, the Pd_2Sn-SP NRs were chosen for evaluating the photothermal performance. A notable laser power density-dependent photothermal effect was observed in Supplementary Fig. 9, and the temperature of Pd_2Sn-SP NRs irradiated with laser (0.8 W cm^{-2}) can considerably increase by 26 °C, which is sufficient for killing cancer cells. It is noteworthy that the temperature change of Pd_2Sn-SP NRs also showed concentration-dependent (Fig. 3c), while only a slight increase of pure water with laser excitation (0.8 W cm^{-2}), which was

https://doi.org/10.1038/s41467-024-53135-2

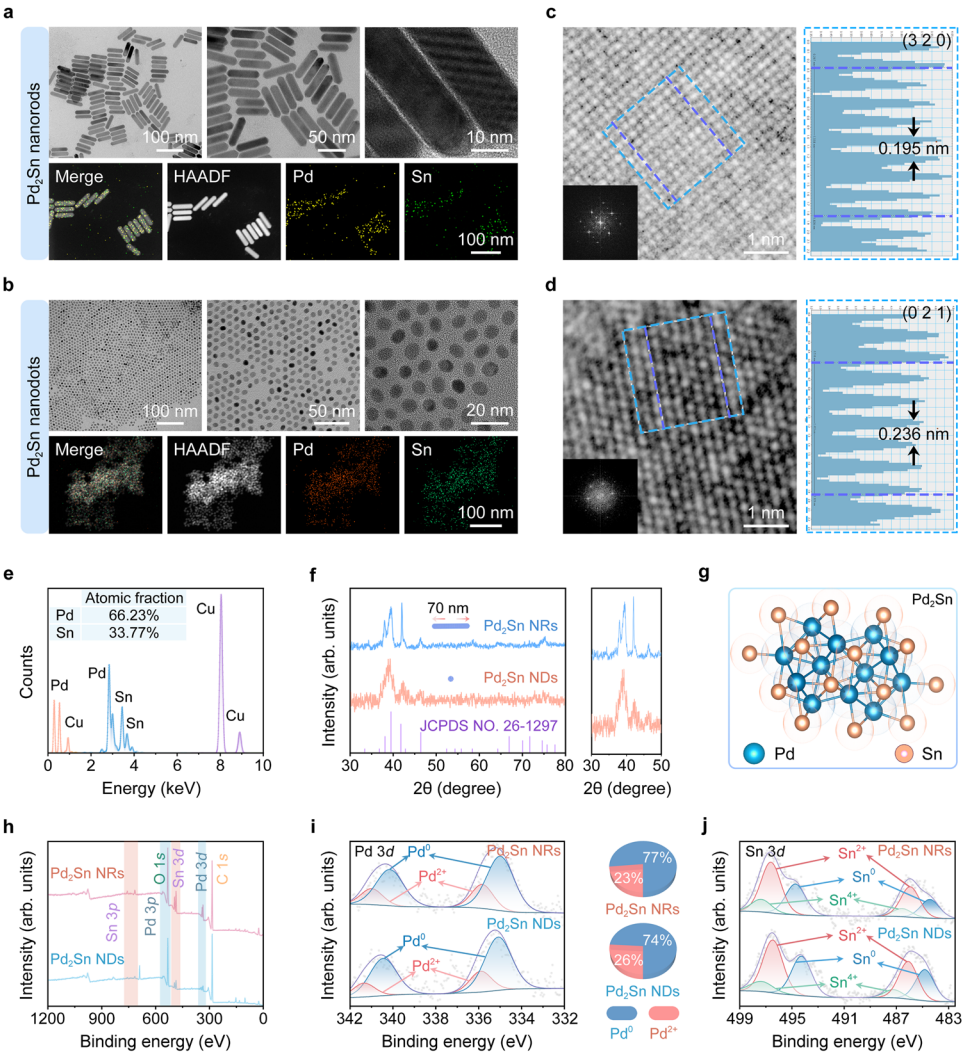

Fig. 2 | Structural and compositional characterization. TEM images at different magnifications and corresponding elemental mapping of **a** Pd_2Sn NRs and **b** Pd_2Sn NDs. High-resolution TEM images and lattice spacing measurement of **c** Pd_2Sn NRs and **d** Pd_2Sn NDs. One representative data was shown from six independently repeated experiments. **e** EDS spectrum of Pd_2Sn NRs. **f** PXRD patterns, **g** crystal structure, **h** XPS survey spectra, and **i**, **j** high-resolution XPS spectra of Pd 3*d* and Sn 3*d* for Pd_2Sn NRs and Pd_2Sn NDs. Source data are provided as a Source Data file (arb. units arbitrary units).

also verified from the infrared thermal images (Supplementary Fig. 10), indicated the excellent efficiency of Pd_2Sn-SP NRs for photothermal conversion. Besides photothermal conversion capability, photothermal stability is also critical for the photothermal conversion process, which was further assessed by four on/off laser power cycles. No notable changes in temperature even after four cycles of heating and natural cooling, confirming high photothermal stability (Fig. 3d). Then, the photothermal conversion efficiency (η) of Pd_2Sn-SP NRs was calculated to be 41.2% on the basis of cooling phase (Fig. 3e). The high light absorption and excellent photothermal conversion ability of Pd_2Sn-SP NRs make them effective contrast agents for photoacoustic imaging (PAI) due to the LSPR effect[33,34]. Consequently, the in vitro PAI ability of Pd_2Sn-SP NRs was explored by detecting the PA signals of Pd_2Sn-SP NRs with different concentrations. As displayed in Supplementary Fig. 11, the PA signals showed a positive correlation with the concentration of Pd_2Sn-SP NRs, which demonstrated the ideal PAI ability for biomedical and clinical applications.

Taking the excellent catalytic activity for effective anti-cancer treatment into consideration, the multienzyme-mimic activities as well as the cascade catalytic reaction of Pd_2Sn-SP nanocomposites were explored[32,35]. To begin with, the generation of $^1O_2$ and ·OH was quantitatively evaluated by the electron spin resonance (ESR) measurement with 2,2,6,6-tetramethylpiperidine (TEMP) and 5,5-dimethyl-1-pyrroline *N*-oxide (DMPO) as trapping agents (Fig. 3f). An obvious signal peak of $^1O_2$ could be seen when the Pd_2Sn-SP nanocomposites were irradiated with a laser, and the stronger signals occurred after the addition of H_2O_2 (Supplementary Fig. 12a). The distinct quadruple resonance peaks of ·OH could be observed in Fig. 3g, displaying a signal intensity ratio of 1:2:2:1, which was further enhanced upon laser irradiation, indicating the laser-induced hyperthermia-enhanced production of ·OH. Moreover, 9,10-diphenylanthracene (DPA) was further used to confirm the generation of $^1O_2$, the absorption intensity of DPA weakened with time after being exposed to the laser, illustrating the generation of $^1O_2$ by Pd_2Sn-SP nanocomposites (Supplementary Fig. 12b). Simultaneously, the POD-mimic activity of Pd_2Sn-SP NRs was also validated by the color reaction of *o*-phenylenediamine (OPD) and 3,3′,5,5′-tetramethyl-benzidine (TMB), which could be oxidized by ·OH to generate orange (oxOPD) or blue color (oxTMB) with the characteristic peak at ~420 or ~652 nm, respectively. The Pd_2Sn-SP NRs induced remarkable characteristic absorption of oxOPD or oxTMB after adding H_2O_2, while the control or laser alone group showed no changes (Fig. 3h, i). Moreover, the absorption intensity was enhanced when the Pd_2Sn-SP NRs irradiated with a laser, which was similar to the results of ESR measurement.

https://doi.org/10.1038/s41467-024-53135-2

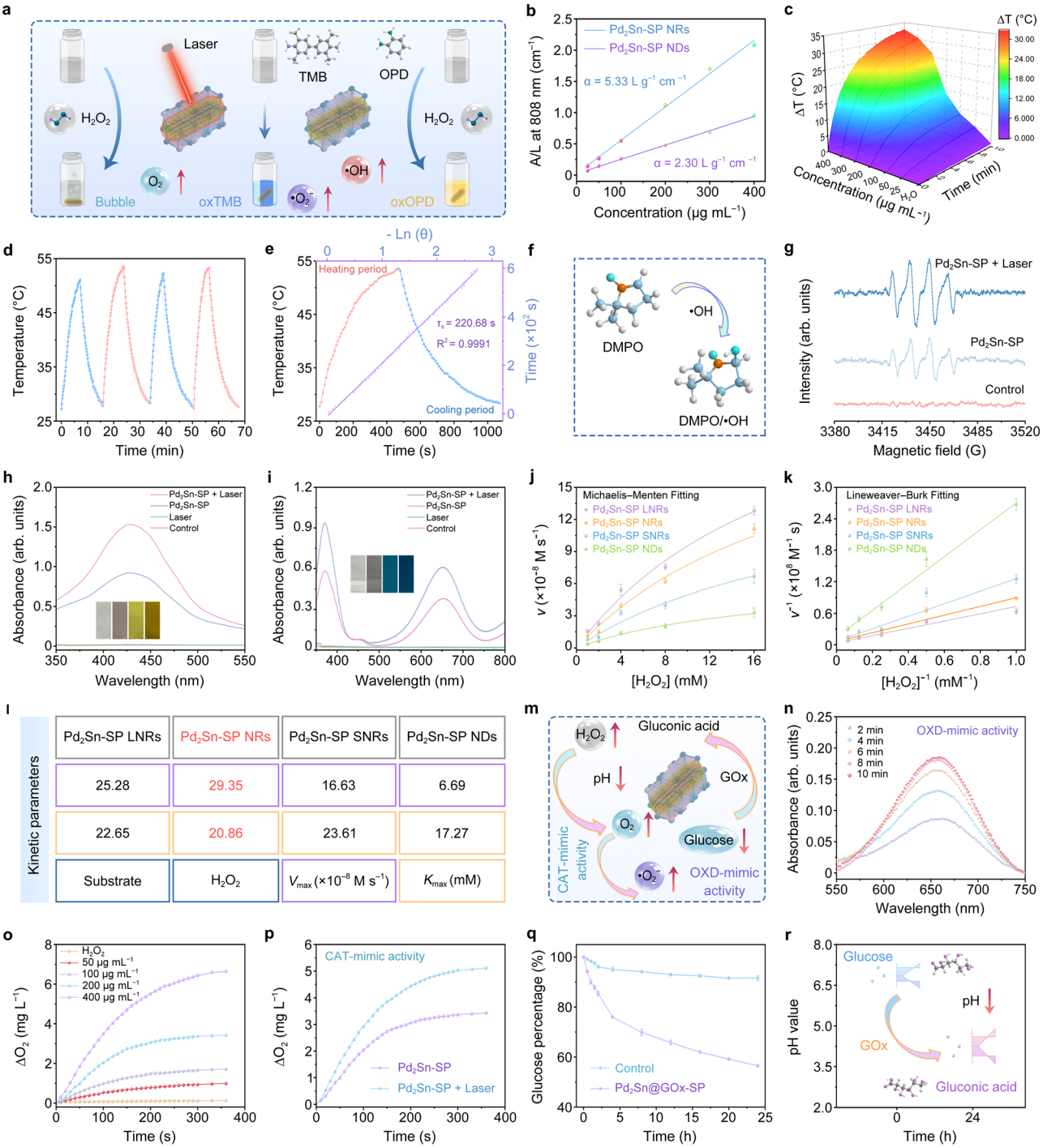

Fig. 3 | Evaluation of photothermal and multi-enzymatic catalytic activity of Pd_2Sn-SP nanocomposites. a Schematic illustration for the detection of photothermal and multi-enzymatic catalytic activity. **b** The fitting curve of the mass extinction coefficient of Pd_2Sn-SP NRs and Pd_2Sn-SP NDs. **c** The concentration-dependent photothermal heating curves, **d** photothermal heating and natural cooling cycles of Pd_2Sn-SP NRs. **e** Photothermal heating and cooling curve and the relationship between −Lnθ and the time. **f**, **g** Diagram and ESR spectra of ·OH with different treatments. UV–vis absorption spectra of **h** OPD and **i** TMB catalyzed by Pd_2Sn-SP NRs under various conditions. **j** Michaelis–Menten kinetic analysis and **k** Lineweaver–Burk plotting for POD-mimic activity of Pd_2Sn-SP nanocomposites. **l** Comparison of the kinetic parameters for POD-mimic activity of Pd_2Sn-SP with different morphologies. **m** Schematic illustration of the mutual promotion of multi-enzyme activity. **n** OXD-mimic activity of Pd_2Sn-SP NRs at various times. Time-dependent O_2 production of Pd_2Sn-SP NRs **o** with different concentrations and **p** with or without laser irradiation. **q** Glucose consumption of Pd_2Sn@GOx-SP. **r** The change of pH value at different times. Data are expressed as mean ± S.D. ($n = 3$) independent experiments in (**h**–**k**, **q**, **r**). Source data are provided as a Source Data file (arb. units arbitrary units).

Furthermore, the difference in catalytic activity of Pd_2Sn-SP nanocomposites with diverse morphology (NDs, NRs, SNRs, and LNRs) was investigated by the steady-state kinetic analyses. Four types of Pd_2Sn-SP nanocomposites were mixed with H_2O_2 at various concentrations (1, 2, 4, 8, and 16 mM), and the absorbance change of oxTMB was recorded with time (Supplementary Fig. 13), all of which could align well with the typical Michaelis–Menten kinetics (Fig. 3j). Based on the Lineweaver–Burk plots (Fig. 3k), the maximum reaction velocity (V_{max}) and Michaelis–Menten constants (K_m) were acquired and summarized in Fig. 3l. Generally, a higher V_{max} and lower K_m lead

to better catalytic performance. Compared with the Pd_2Sn-SP NDs, the Pd_2Sn-SP NRs exhibited higher catalytic efficiency. Moreover, the catalytic efficiency was also relevant to the length of Pd_2Sn-SP NRs, neither too long nor too short is beneficial for the POD-mimic activity. Additionally, Pd_2Sn-SP nanocomposites with diverse morphology were employed to further evaluate the catalytic activity by altering the concentrations of Pd_2Sn-SP nanocomposites and detecting the absorption intensity of oxTMB (Supplementary Fig. 14a–d). The specific activity values of Pd_2Sn-SP nanocomposites were calculated (Supplementary Fig. 14e–h) and summarized in Supplementary Fig. 14i. Similarly, the Pd_2Sn-SP NRs showed the supreme POD-mimic catalytic activity than the others. The effective generation of ·OH in the presence of Pd_2Sn-SP NRs was also confirmed by performing a methylene blue (MB) experiment. As displayed in Supplementary Fig. 15, the absorbance of MB decreased with the prolonged reaction time, demonstrating the excellent generation ability of ·OH. In addition to ·OH, the $\cdot O_2^-$ generation based on the oxidase (OXD)-mimic catalytic activity of Pd_2Sn-SP NRs was also validated using TMB (Fig. 3n). The absorbance intensity at 652 nm increased with a prolonged time, showing the obvious OXD-mimic activity of Pd_2Sn-SP NRs.

Considering the hypoxic TME restricts the OXD-mimic activity, the CAT-mimic catalytic activity of Pd_2Sn-SP NRs by catalyzing H_2O_2 into O_2 was detected. The Pd_2Sn-SP nanocomposites with diverse morphology were added with various concentrations of H_2O_2 and the oxygen content was recorded for comparison. As shown in Supplementary Fig. 16, all the Pd_2Sn-SP nanocomposites could produce more O_2 with the increase of H_2O_2 concentration, and Pd_2Sn-SP NRs displayed the strongest CAT-mimic catalytic activity, which was consistent with the results of POD-mimic catalytic activity. In addition, the generation of O_2 also increased with the concentration of Pd_2Sn-SP NRs (Fig. 3o), and the addition of laser further promoted the CAT-mimic catalytic activity (Fig. 3p). Although the TME is featured by the overexpression of H_2O_2, the endogenous H_2O_2 content is unable to meet the subsequent biocatalytic reactions[36]. Thus, the Pd_2Sn-SP NRs were modified with GOx to supply H_2O_2 by catalyzing glucose decomposition. The catalytic ability of Pd_2Sn@GOx-SP for accelerating glucose consumption was verified, the glucose consumption increased with the prolonged reaction time, while the negligible change was observed in the control group (Fig. 3q). Meanwhile, the degradation of glucose is accompanied by the production of gluconic acid, leading to the reduction of pH value (Fig. 3r). Therefore, the consumption of endogenous glucose could not only provide H_2O_2 for enzyme-catalyzed reaction, but also reduce pH value to enhance the enzyme catalytic efficiency. Furthermore, the catalytic activity of GOx was evaluated in PBS with different pH values to investigate whether the GOx would malfunction in a more acidic environment. The results showed that there was no obvious change in the catalytic performance of GOx in a more acidic environment, demonstrating that the GOx was able to effectively degrade glucose and afford H_2O_2 for the cascade catalytic reaction (Supplementary Fig. 17). Moreover, the O_2 generated by CAT-mimic catalytic activity could also improve the OXD-mimic activity as well as the glucose consumption by GOx, achieving mutual promotion and common improvement (Fig. 3m). We also evaluated the influence of pH value on the etching and leaking of Sn and Pd ions by using inductively coupled plasma-optical emission spectrometry (ICP-OES). As shown in Supplementary Fig. 18, the Sn and Pd ions could be released from Pd_2Sn@GOx-SP, while the amount of ion release was negligible even during 3 days of incubation, which was only 2.73 and 1.10 μg mL^{-1}, respectively. The ability to reshape the TME and promote the extensive generation of ROS endows Pd_2Sn@GOx-SP with excellent potentiality for tumor therapy.

DFT calculations and enzymatic catalysis mechanism

DFT calculations were further performed to unveil the catalytic mechanism and the crystal-facet-dependent multienzyme-mimicking activities of Pd_2Sn. First, the bulk structure of Pd_2Sn was optimized and displayed in Fig. 4a. According to the calculated density of states (DOS) in Fig. 4b, it can be identified that the predominant contribution of the DOS near the Fermi level originated from Pd-5*d* orbitals, indicating that electrons near the Fermi level are mainly provided by Pd atoms and of great importance for the catalytic activity of Pd_2Sn. The moderate atomic radius and *d* orbitals with abundant electrons of the Pd made Pd_2Sn easy to interact with the reactant molecules and promote the electron transfer process. Thus, the excellent catalytic activities of Pd_2Sn could be achieved by activating the reactants and subsequently forming suitable intermediates with lower energy barriers. Based on the facet discrepancy of Pd_2Sn NDs and NRs, three surface models with exposed (001), (010), and (011) crystal facets were built to clarify the enzyme catalytic mechanisms (Fig. 4c). Before evaluating the catalytic activity of different Pd_2Sn facets, microscopic electron structures and Bader charge analysis were conducted to observe the charge distribution. As shown in Fig. 4d, the surface electrons were transferred from Sn to Pd atoms, which altered the redistribution of electrons and led to the negative valence state of Pd. It can be observed clearly that the charges of the Pd sites on (001), (101), and (011) surfaces were calculated to be −0.297, −0.418/−0.484, and −0.261/−0.339/−0.348 e, respectively. The significant change of surface electron density could have an impact on the catalytic performance of Pd_2Sn catalysts, as discussed in detail later.

Furthermore, to evaluate the electron transfer behavior between the catalyst surface and the intermediates, the work functions of different facets were also calculated[37]. In response to the surface charge redistribution, the data in Fig. 4e–g identified that the work functions for (001), (010), and (011) facets are 6.902, 6.341, and 7.241, indicating the electron transfer from the catalyst surface to the intermediates followed by the sequence of (010) > (001) > (011). In addition, the adsorption process of H_2O and H_2O_2 on the Pd and Sn sites of different Pd_2Sn facets was analyzed and summarized in Supplementary Fig. 19a. The adsorption energy of H_2O_2 on Pd and Sn sites of three different crystal facets were much lower than that of H_2O, which was beneficial for its preferential adsorption thus the subsequent catalysis (Supplementary Fig. 19b). Significantly, the corresponding adsorption energies of H_2O_2 on Pd site in (001), (010), (011) facets were calculated to be −0.28, −0.17, and −0.13 eV, respectively. The lower adsorption energy of H_2O_2 on the Pd site with respect to the Sn site in the (001) facet ensured the energetically favorable binding of H_2O_2 on the catalyst surface.

Furthermore, to reveal the relevant catalytic mechanism, three optimized surfaces of Pd_2Sn were adopted to comprehensively investigate the H_2O_2 catalytic process. The critical intermediates formed in the successive reaction steps of CAT-mimic and POD-mimic activities were displayed in Fig. 4h and Supplementary Fig. 19c. All the H_2O_2 catalytic reaction intermediates were optimized for the (001), (010), and (011) crystal facets. Regarding the POD-mimic activity, the calculated energy profiles are illustrated in Fig. 4i and Supplementary Fig. 19d. The first step involves the capture and surface adsorption of H_2O_2 on the Pd_2Sn surface. Then, the H_2O_2 was decomposed into two OH*, which was thermodynamically favorable in the three crystal facets. In the third step, the adsorbed OH* was released and formed ·OH, which required to overcome an energy barrier and thus became the rate-determining step. Pd sites on the (001) facet possessed the lowest free energy (2.59 eV per OH*) for the desorption of bridged OH* intermediate compared with (010) and (011) crystal facets (2.73 and 2.63 eV per OH*, respectively), demonstrating its better POD-mimic activity.

Simultaneously, the energy profiles for the CAT-mimic activity were shown in Fig. 4j and Supplementary Fig. 19e. Five successive catalytic processes on the (001), (010), and (011) crystal facets have been calculated. The adsorption, activation, and dissociation of H_2O_2 were all exothermic in all crystal facets, indicating the feasibility of the

https://doi.org/10.1038/s41467-024-53135-2

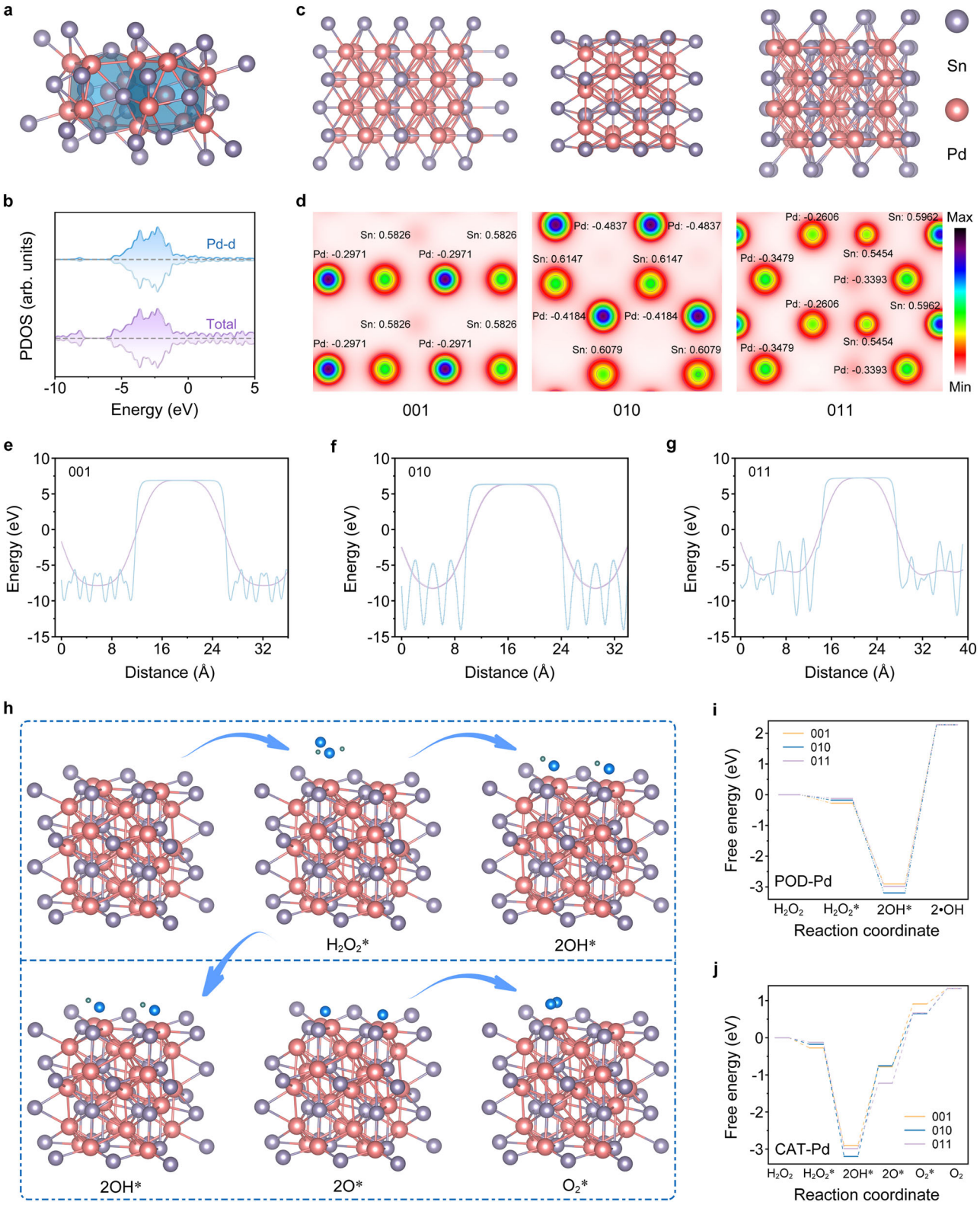

Fig. 4 | DFT calculations and enzyme catalytic mechanism. a Polyhedral view of the optimized structure of Pd_2Sn. The red and purple balls represent the Pd and Sn atoms. **b** Density of states of Pd_2Sn. **c** Optimized structural models of Pd_2Sn with different crystal facets and **d** the corresponding electron density mapping images (the effective charges were obtained by the Bader analysis program). **e**–**g** Calculated potential profile averaged on the plane perpendicular to the *c*-axis of Pd_2Sn with different crystal facets. **h** The reaction pathways and **i**, **j** the corresponding energy profiles for the POD- and CAT-mimic activities on Pd sites of Pd_2Sn with different crystal facets. Source data are provided as a Source Data file (arb. units arbitrary units).

reaction process. Conversely, the deprotonation of OH* to form O* and the subsequent formation of bridge structure O_2* were apparent endothermic processes. For the Pd site on Pd_2Sn (001) surface, the energies required to form O* and O_2* intermediates are calculated to be 1.06 eV (deprotonation of one H) and 1.69 eV, respectively. In contrast, relevant values for Pd_2Sn (010)/(011) surfaces are 1.22/1.41 and 0.88/1.89 eV. Moreover, the deprotonation of OH* on the Pd_2Sn (001) surface is much easier than that on the Pd_2Sn (010) surface, while the energy required to form O_2* on the Pd_2Sn (010) surface is the lowest. Thus, the formation of O_2* intermediates became the rate-determining step in the catalytic processes of CAT-mimic activity. It should be noted that the deprotonation of OH* to produce hydrogen products (H_2) required an electron transfer between catalyst surface and intermediates. Therefore, the highest work function of (011) facet would result in the highest interfacial charge transfer resistance during this fundamental step, even the (011) facet exhibited a much lower energy barrier. In addition, as all the energy barriers needed to overcome for Pd sites on (001) and (010) surface are significantly lower than the one (1.89 eV) to form O_2* on (011) surface, demonstrating the CAT-mimic activity of the Pd_2Sn (011) surface is the worst.

According to Supplementary Fig. 19f, it can be further confirmed that the energy barrier for the formation of O_2* at Pd sites is well correlated with the work function of different facets, implying that the charge redistribution caused by the change of the surface orientation will alter the electronic structure of the catalyst surface, and thus changing the reaction mechanism. In addition, the results in Supplementary Fig. 19g also indicated that the Sn sites in the three facets do not exhibit obvious superiority over the formation of O* and O_2* intermediates, but they are favorable for the desorption of O_2 with the energies ranging from −0.19 to 0.10 eV. According to the analysis on the adsorption, reaction, and desorption capabilities of different sites on different facets, it can be concluded that Pd and Sn sites play different but synergistic roles in determining the overall activity during whole CAT-mimic reaction. In brief, the POD-mimic activity is easier to occur in (001) crystal facet than in (011) crystal facet. The (001) and (010) crystal facets play different roles in CAT-mimic activity, in which (001) facet facilitates the deprotonation of OH* and (010) facet facilitates the formation of O_2*. Both (001) and (010) crystal facets exhibit better CAT-mimic activity than (011) crystal facets. Moreover, Sn sites facilitate the desorption of O_2, collaboratively promoting the CAT-mimic activity. Overall, the CAT-mimic and POD-mimic activities of Pd_2Sn were theoretically verified by the exploration of the reaction pathways and energy profiles, further demonstrating that the Pd_2Sn NRs with exposed (001) facet possessed higher catalytic activity than Pd_2Sn NDs with exposed (011) facet.

In vitro synergistic pyroptosis and disulfidptosis

These experiments have confirmed that the Pd_2Sn@GOx-SP possessed the property for altering the TME and generating abundant ROS. We further evaluated the in vitro anti-tumor therapeutic effect of Pd_2Sn@GOx-SP (Fig. 5a). To begin with, we measured the cytotoxicity of Pd_2Sn@GOx-SP on CT26 cells by methylthiazolyldiphenyl-tetrazolium bromide (MTT) assay. Various concentrations of Pd_2Sn-SP and Pd_2Sn@GOx-SP were co-incubated with CT26 cells in the dark to detect the dark-toxicity, and the photo-toxicity of Pd_2Sn@GOx-SP was detected by laser irradiation followed by the incubation. As can be seen in Fig. 5b, both Pd_2Sn-SP and Pd_2Sn@GOx-SP were cytotoxic to CT26 cells compared with drug-free incubation. Significantly, the Pd_2Sn@GOx-SP exhibited remarkable photo-toxicity on tumor cells under laser irradiation. Moreover, the cytotoxicity of Pd_2Sn@GOx-SP nanocomposites on normal cells and multiple cancer cells was further performed to evaluate the tumor growth inhibitory effect. Our findings revealed that the nanocomposites showed varying degrees of inhibitory effects on cancer cells (Supplementary Fig. 20a). While for normal cells (L929 and 3T3 cells), both Pd_2Sn-SP and Pd_2Sn@GOx-SP were almost non-cytotoxic after co-incubation of 12 and 24 h, showing good biocompatibility even at higher concentrations (Supplementary Fig. 20a–d). Given the existence of TOP on the surface of Pd_2Sn, we further co-cultured the L929 cells with TOP at different concentrations to evaluate the biotoxicity of P originated from TOP. The result showed no significant toxic side effects on L929 cells, demonstrating the negligible biotoxicity of P in TOP (Supplementary Fig. 20e). Meanwhile, the influence of Sn and Pd ions leaking on L929 cells was also investigated through MTT assay by co-culturing the released Sn and Pd ions with L929 cells. The results showed that there was no obvious biotoxicity on L929 cells (Supplementary Fig. 20f), indicating the high biosafety of Pd_2Sn@GOx-SP. Thus, the nanocomposites exhibited negligible cytotoxicity on normal cells without laser irradiation, demonstrating high selective toxicity. To explore the cellular internalization performance of Pd_2Sn@GOx-SP, the cancer cells incubated with fluorescein isothiocyanate (FITC) modified Pd_2Sn@GOx-SP were analyzed by confocal laser scanning microscopy (CLSM) and flow cytometry, respectively (Fig. 5c, d and Supplementary Fig. 21a, b). The cells treated with FITC-labeled Pd_2Sn@GOx-SP showed higher fluorescence over a prolonged incubation time, exhibiting the excellent cellular uptake efficiency of Pd_2Sn@GOx-SP.

Research has shown that endocytosis is the main internalization process of nanocomposites, and the uptake rate of rod-like nanocomposites was higher than that of spherical nanocomposites[38–40]. The endosomes/lysosomes usually play an indispensable role in transporting and releasing nanocomposites during subsequent intracellular processes[41]. Consequently, the endosomal escape process of Pd_2Sn@GOx-SP was evaluated by staining lysosomes with Lyso-Tracker. The results revealed that the FITC-labeled Pd_2Sn@GOx-SP was colocalized with lysosomes within 1 h after internalization (Pearson's correlation coefficient of 0.79). With the extension of incubation time, the Pd_2Sn@GOx-SP gradually escaped from the lysosomes, as evidenced by the Pearson's correlation coefficient was decreased to 0.52 and 0.39 after 2 and 4 h of internalization, respectively (Fig. 5c), indicating that the Pd_2Sn@GOx-SP could effectively escape from endolysosomes. Considering stereoscopic structure of the tumor, we further investigated the penetration performance of Pd_2Sn@GOx-SP on CT26 multicellular spheroids to simulate three-dimensional tumors. Similarly, the fluorescence intensity of multicellular spheroids incubated with FITC-labeled Pd_2Sn@GOx-SP enhanced with the time prolongs (Supplementary Fig. 21c), indicating the ideal permeability for the multicellular spheroids. Thus, the ideal penetration ability could promote the accumulation of Pd_2Sn@GOx-SP in solid tumors, which could gain more access to tumor cells and improve the therapeutic efficacy.

Subsequently, the change of intracellular substances and their effect on cell death was further evaluated on CT26 cells. The oxygen content in tumor cells plays a significant role in tumor therapy[42]. On the one hand, the generated O_2 could accelerate the consumption of glucose in the presence of GOx to trigger a series of cellular damage. On the other hand, the abundant O_2 could be converted into $^1O_2$ and $\cdot O_2^-$ catalyzed by Pd_2Sn@GOx-SP, which enhances the oxidative damage of tumor cells. $[Ru(dpp)_3]^{2+}Cl_2$ as an oxygen detection probe was used to evaluate the oxygen production of Pd_2Sn@GOx-SP in CT26 cells. As displayed in Fig. 5e, different from the control and laser groups, the red fluorescence intensity of the cells decreased after incubation with Pd_2Sn-SP, suggesting that the continuous production of O_2 based on the CAT-mimic catalytic activity of the Pd_2Sn-SP. It was also comparatively found that the cells in the Pd_2Sn@GOx-SP group exhibited a brighter red fluorescence than that of Pd_2Sn-SP, which could be attributed to the O_2 consumption in the decomposition of glucose by GOx. Whilst, a large amount of H_2O_2 generation is accompanied by the process of glucose decomposition, which could further augment the content of ROS. It has been confirmed that the abnormal increase of intracellular ROS levels could induce damage to crucial

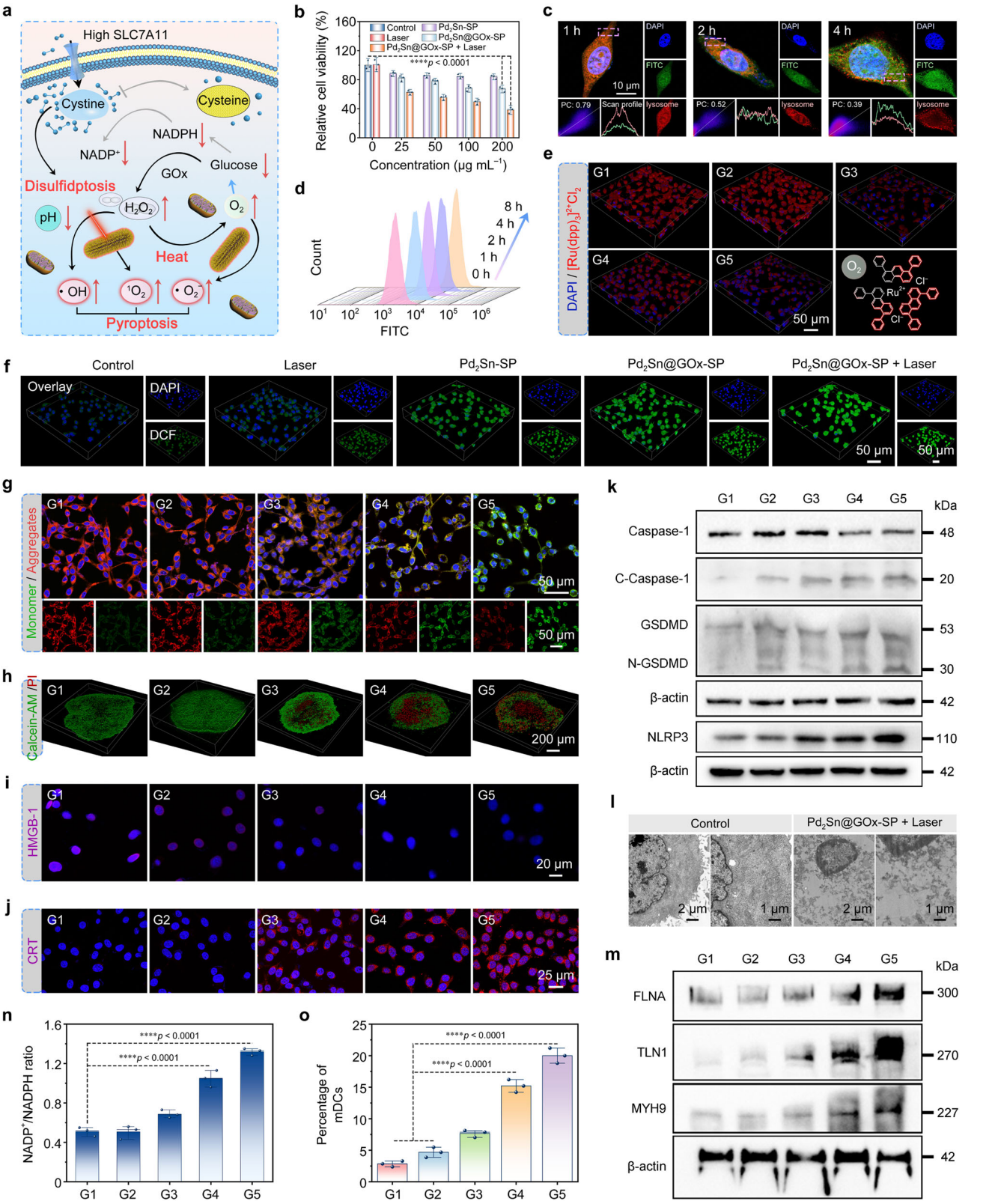

cellular biomolecules, leading to cell death (including pyroptosis) through the Caspase-1/GSDMD pathway[43,44]. Various strategies to generate ROS have been confirmed in vitro and showed excellent anti-tumor therapeutic potential[45]. Thus, the intracellular ROS was determined by CLSM and flow cytometry using a 2′,7′-dichlorofluorescein diacetate (DCFH-DA) probe (Fig. 5f and Supplementary Fig. 21d, e). The results showed the fluorescence intensity of Pd_2Sn@GOx-SP group was remarkable, demonstrating the exceptional ability of ROS generation. Especially, the highest fluorescence intensity was observed in the Pd_2Sn@GOx-SP + laser group due to the enhancement of ROS generation by the hyperthermia effect.

High levels of ROS in tumor cells could achieve irreversible damage to DNA to induce pyroptosis[46]. Considering the abnormal elevated ROS levels could lead to mitochondrial dysfunction, the

Fig. 5 | In vitro synergistic pyroptosis and disulfidptosis. a Schematic illustration of the synergistic pyroptosis and disulfidptosis mediated by Pd_2Sn@GOx-SP. **b** Cytotoxicity assays of CT26 cells with different treatments. **c** Representative CLSM images of the colocalization of FITC-labeled Pd_2Sn@GOx-SP with the lysosome. **d** Flow cytometry profile of FITC-labeled Pd_2Sn@GOx-SP in CT26 cells. CLSM images of intracellular **e** O_2 generation and **f** ROS level after various treatments (G1, control; G2, laser; G3, Pd_2Sn-SP; G4, Pd_2Sn@GOx-SP; G5, Pd_2Sn@GOx-SP + laser). **g** JC-1 staining of CT26 cells with diverse treatments. **h** Calcein-AM/PI staining of CT26 multicellular spheroids. Fluorescence image of **i** HMGB1 migration and **j** CRT exposure of CT26 cells with diverse treatments. **k** Western blot analysis of Caspase-1, C-Caspase-1, GSDMD, N-GSDMD, and NLRP3 in CT26 cells after diverse treatments. **l** Bio-TEM images of CT26 cells with diverse treatments. **m** Western blot analysis of FLNA, TLN1, and MYH9 in CT26 cells after diverse treatments. **n** Measurement of the $NADP^+$/NADPH ratio. **o** The quantitative data of matured DCs after diverse treatments by in vitro stimulation maturation experiment. Data are expressed as mean ± S.D. ($n = 3$) independent samples in (**b**, **n**, **o**). Statistical significance is assessed by a two-way ANOVA with Tukey's multiple comparisons test. Source data are provided as a Source Data file (one representative data was shown from three independently repeated experiments).

change of mitochondrial membrane potential after various treatments was evaluated by performing JC-1 staining. As shown in Supplementary Fig. 21f, JC-1 forms aggregates within the matrix of mitochondria under normal polarization conditions, exhibiting vibrant red fluorescence. On the contrary, JC-1 could only exist as a monomer in depolarized mitochondria, showing green fluorescence[46]. As depicted in Fig. 5g, intense red fluorescence was shown in the cells with the treatment of control and only laser, indicating normal mitochondria. In particular, the green fluorescence intensity of cells treated with Pd_2Sn@GOx-SP increased significantly, and the highest green–red fluorescence proportion was exhibited in the Pd_2Sn@GOx-SP + laser group, demonstrating severe mitochondrial damage. Meanwhile, highly toxic ROS could analogously destroy the lysosomes[47], which are also crucial subcellular organelle. The integrity of lysosomes was analyzed by acridine orange staining assay, in which red fluorescence could change into green fluorescence when the lysosome ruptured. The results showed that the lysosomal membrane integrity was completely ruptured after the treatment of Pd_2Sn@GOx-SP + laser, and a certain rupture could also be observed in the Pd_2Sn-SP and Pd_2Sn@GOx-SP groups (Supplementary Fig. 22a).

The destruction of Pd_2Sn@GOx-SP on CT26 cells was also confirmed by observing the morphological changes of actin filaments (F-actin). The cytoskeletal disruption could be seen in the cells after being treated with Pd_2Sn@GOx-SP, while the F-actin of the cells in the group of control or only laser were highly elongated and well-organized (Supplementary Fig. 22b), demonstrating the cell injury induced by Pd_2Sn@GOx-SP. To gain further insights into the living and dead cells, Calcein-AM/PI was used to stain the cells in various groups, and the fluorescence intensity was examined (Supplementary Fig. 22c). The dead cells in the control or only laser group were negligible, while dead cells predominated in the group of Pd_2Sn@GOx-SP + laser, indicating the strong killing efficiency of Pd_2Sn@GOx-SP on tumor cells. The living and dead cells proportion in different treatment groups was also obtained by flow cytometric assay. The dead cells increased after treatment with Pd_2Sn-SP or Pd_2Sn@GOx-SP, and the cell mortality rate reached its maximum after incubation with Pd_2Sn@GOx-SP + laser (Supplementary Fig. 22d), suggesting the ideal treatment effect of Pd_2Sn@GOx-SP on cancer cells. Besides that, we also investigated the therapeutic performance of Pd_2Sn@GOx-SP on CT26 multicellular spheroids in vitro. Consistent with the above results, almost no cell death was observed in control or only laser groups, while a certain amount of dead cells existed in Pd_2Sn@GOx-SP group, and a significant increase of dead cells was found in Pd_2Sn@GOx-SP + laser group (Fig. 5h). Different depths of cell death could be observed, confirming the effective ability for tumor inhibition.

After confirming the excellent capability for killing tumor cells, we further explored the specific mechanism of Pd_2Sn@GOx-SP-induced cell death in detail. Due to the massive production of ROS with various types, we speculated that Pd_2Sn@GOx-SP could induce pyroptosis[46,48,49]. As an inflammatory programmed cell death, pyroptosis could activate the anti-tumor immune responses by releasing various inflammatory factors, which could serve as an important means to improve immune deficiencies[25]. To verify the immune activation effect induced by Pd_2Sn@GOx-SP, the typical biomarkers of immunogenic cell death (ICD), high mobility group 1 (HMGB1) and calreticulin (CRT) were detected by immunofluorescence assay. As can be seen in Fig. 5i, strong red fluorescence overlapped with the cell nucleus in control and only laser groups, while that was diminished in the Pd_2Sn@GOx-SP and Pd_2Sn@GOx-SP + laser groups, indicating that Pd_2Sn@GOx-SP could trigger pyroptosis and release HMGB1 into the extracellular milieu. Meanwhile, more CRT expression was detected on the cellular surface in the Pd_2Sn@GOx-SP and Pd_2Sn@GOx-SP + laser groups, whereas no significant signal in the control or only laser group (Fig. 5j). Moreover, the cells treated with drugs showed significant adenosine triphosphate (ATP) release, wherein the leakage level of the Pd_2Sn@GOx-SP + laser group was the highest compared with other groups (Supplementary Fig. 22e). All results clearly validated that Pd_2Sn@GOx-SP could induce large-scale ICD effects mediated by pyroptosis.

Furthermore, western blot analysis was also initiated to assess protein expression during the pyroptosis process (Fig. 5k). In the pyroptotic pathway, NLRP3 inflammasome and Caspase-1 could be stimulated by abundant ROS and GOx, and subsequently achieve the cleaving of GSDMD into N-GSDMD, which could lead to the perforation of the cellular membranes[49]. The high expression of NLRP3 could be observed in the group treated with Pd_2Sn@GOx-SP due to the two-pronged strategy. In addition, the Pd_2Sn@GOx-SP-related group exhibited high expression of Cleaved Caspase-1 (C-Caspase-1) and N-GSDMD proteins, which could underpin the drilled pores in cell membrane, leading to the secretion of damage-associated molecular patterns. To further confirm the GSDMD- or NLRP3-dependent pyroptosis induced by Pd_2Sn@GOx-SP + laser, we have knocked down the expression of GSDMD or NLRP3 in CT26 cells, then the cytotoxicity of Pd_2Sn@GOx-SP + laser on the treated CT26 cells was measured. To begin with, transient transfection was performed to establish GSDMD or NLRP3 knockdown CT26 cells, respectively. The transfection efficiency was verified by western blot analysis (Supplementary Fig. 22f). And the experimental results verified that CT26 cells with low expression of GSDMD or NLRP3 had higher cell viability than the control group after being treated with Pd_2Sn@GOx-SP + laser, respectively (Supplementary Fig. 22g). Thus, the pyroptosis could be achieved by the treatment of Pd_2Sn@GOx-SP + laser, which is dependent on the GSDMD and NLRP3. Considering the results in immunofluorescence and western blot analysis, we attempted to offer in-depth evidence of pyroptosis induced by Pd_2Sn@GOx-SP. In the most intuitive way, the cell morphology after various treatments was recorded. As can be seen in Supplementary Fig. 22h, CT26 cells with the treatment of Pd_2Sn@GOx-SP possessed more distinct swelling (bubbling) features compared with those in the control group, indicating the occurrence of pyroptosis. Meanwhile, Bio-TEM was also performed to monitor the cells with the different treatments (Fig. 5l). It can be observed that the cell membrane of the cells treated with Pd_2Sn@GOx-SP exhibited extensive vacuolization and incomplete cell membranes, and mitochondria were deformed and swollen. These results provide concrete evidence for Pd_2Sn@GOx-SP-induced pyroptosis due to a large amount of ROS generation.

Significantly, the tumor cells exhibited high levels of SLC7A11, which could import cystine to promote GSH synthesis and resist

pyroptosis[50]. Considering that we introduced GOx to constrict that process by consuming glucose, which could deplete the NADPH to prevent the reduction of cystine, achieving the inhibition of GSH synthesis. The quantitative evaluation of intracellular glucose was conducted, the cells treated with GOx exhibited the obvious consumption of glucose (Supplementary Fig. 22j). In addition, the aberrant buildup of intracellular cystine could lead to disulfide stress, which ultimately induces disulfidptosis (Fig. 5a). To begin with, we performed non-reducing western blots to validate glucose starvation could induce disulfide-bond formation in the actin cytoskeleton proteins. As shown in Fig. 5m, the actin cytoskeleton proteins (FLNA, TLN1, and MYH9) in CT26 cells exhibited slower migration on the smears following treatment with Pd_2Sn@GOx-SP. Some of these proteins displayed exceptionally high-molecular-weight bands near the stacking layer, whereas the control or laser-only groups did not show similar migration patterns, indicating that the actin cytoskeleton proteins formed multiple intermolecular disulfide bonds under the treatment of Pd_2Sn@GOx-SP. Subsequently, we evaluated the NADPH levels by performing various treatments on CT26 cells. As depicted in Fig. 5n, the cells handled with Pd_2Sn@GOx-SP exhibited a significant increase in the $NADP^+$/NADPH ratio (which indicates NADPH depletion) due to glucose starvation. In addition, the intracellular GSH levels after various treatments were also assessed. After the treatment of Pd_2Sn@GOx-SP, the GSH levels were obviously decreased (Supplementary Fig. 22k), which could enhance the pyroptosis process.

To further confirm the disulfidptosis induced by Pd_2Sn@GOx-SP + laser, the dithiothreitol (DTT) as disulfidptosis inhibitor was added to the cells, and the cell viability was analyzed by CCK-8 assay. The results showed that the cell viability of the cells added with DTT was obviously higher than that in the absence of DTT after being treated with Pd_2Sn@GOx-SP + laser (Supplementary Fig. 22l), demonstrating the disulfidptosis could be triggered by Pd_2Sn@GOx-SP. Meanwhile, to confirm the critical role of SLC7A11-mediated cystine uptake for disulfide stress, the CT26 cells were incubated with Pd_2Sn@GOx-SP + laser after the treatment of SLC7A11 inhibitor (Erastin). Compared with that without the treatment of Erastin, the cell death rate of CT26 cells exhibited an obvious decrease due to the inhibition of SLC7A11-mediated cystine uptake (Supplementary Fig. 22m), indicating that the disulfide stress originated from the accumulation of cystine mediated by SLC7A11. In addition, the expression levels of SLC7A11 in multiple cancer cells (4T1, HeLa, SW1990, A549, and HepG2 cells) and normal cells (L929 cells) were evaluated by western blot analysis (Supplementary Fig. 22i). The results showed the higher expression level of SLC7A11 in these cancer cells than that in normal cells, leading to higher cell mortality in cancer cells compared to normal cells with low SLC7A11 expression.

Besides that, the CT26 cells were treated with ferroptosis inhibitor (Ferrostatin-1) to give insight into the role of ferroptosis in this work. The result showed that the CT26 cells treated with Pd_2Sn@GOx-SP + laser also exhibited significant inhibitory effect after the addition of Ferrostatin-1, which was similar to that without addition of Ferrostatin-1, demonstrating the effect of ferroptosis could be ignored (Supplementary Fig. 22n). Therefore, GOx-induced disulfidptosis combined with Pd_2Sn@GOx-SP-induced pyroptosis are the main manner for promoting tumor cell death. Furthermore, we also examined whether the Pd_2Sn@GOx-SP + laser treatment could alleviate cell migration by wound-healing assays (Supplementary Fig. 23a). Indeed, cell migration was largely inhibited after treatment with Pd_2Sn@GOx-SP + laser for 12 and 24 h, while the control or only laser group had minimal effect on the cell migration (Supplementary Fig. 23b). Moreover, the transwell migration assay of CT26 cells after diverse treatments was also performed to evaluate the migration ability. Similarly, the cells treated with Pd_2Sn@GOx-SP + laser were greatly repressed (Supplementary Fig. 23c), illustrating that Pd_2Sn@GOx-SP had a significant inhibitory effect on cell migration. Therefore, GOx-induced disulfidptosis combined with Pd_2Sn@GOx-SP-induced pyroptosis greatly promoted tumor cell death and inhibited its migration. To confirm the role of pyroptosis on the augmenting of immunogenicity, the maturation degree of dendritic cells (DCs) was analyzed by flow cytometry analysis, which could improve the antigen presentation ability and initiate the subsequent anti-tumor cascade immunity[51,52]. The results showed that the Pd_2Sn@GOx-SP combined with laser irradiation can significantly increase the proportion of $CD80^+CD86^+$ cells (Fig. 5o and Supplementary Fig. 23d), indicating that Pd_2Sn@GOx-SP treated tumor cells could stimulate DCs activation and facilitate anti-tumor immune responses.

In vivo PA/CT imaging-guided synergistic anti-tumor therapy

The results of in vitro cell experiments validated that the Pd_2Sn@GOx-SP + laser irradiation treatment group resulted in pyroptosis and disulfidptosis. Prior to evaluating the curative effect of the tumor in vivo, the PA/CT imaging capability was assessed based on the ideal light absorption and high X-ray attenuation coefficient (Fig. 6a)[53,54]. To evaluate the potential of Pd_2Sn@GOx-SP for PA imaging, Pd_2Sn@GOx-SP was intravenously (i.v.) injected into CT26-bearing mice, and then imaged at different time intervals by a Vevo LAZR-X system. As presented in Fig. 6b, the PA signals reached the strongest at 6 h post-injection, and subsequently weakened owing to the elimination of Pd_2Sn@GOx-SP from tumor tissues. Meanwhile, the biodistribution of Pd_2Sn@GOx-SP in main organs was also detected by ex vivo PA imaging at 6 h post-injection (Supplementary Fig. 24a), showing the highest accumulation of Pd_2Sn@GOx-SP in the liver compared with other organs. In addition, the blood oxygen saturation (SaO_2) in the tumor was monitored at various times (Supplementary Fig. 24b). The results showed the efficient oxygen supply ability of Pd_2Sn@GOx-SP for glucose consumption by GOx, which is beneficial to the in vivo cascade reaction process.

Similarly, the CT imaging ability of Pd_2Sn@GOx-SP was also investigated both in vitro and in vivo. As presented in Supplementary Fig. 24c, the CT signal intensity gradually strengthened as the concentration of Pd_2Sn@GOx-SP increased. Moreover, the Hounsfield unit (HU) value was positively correlated to the concentration of Pd_2Sn@GOx-SP with a slope of 21.75 (Supplementary Fig. 24d). Thereafter, the CT26-bearing mice were intratumorally (i.t.) and i.v. injected with Pd_2Sn@GOx-SP to evaluate the CT imaging capability, respectively. Contrasted with the control group, the tumor tissues of mice injected with Pd_2Sn@GOx-SP presented a high CT density, suggesting an efficient CT imaging capacity (Fig. 6c, d). Furthermore, we performed CT imaging on the same tumor-bearing mouse at different time points after being injected with Pd_2Sn@GOx-SP. Within 6 h, the CT density in the tumor region of the mice i.v. injected with Pd_2Sn@GOx-SP were markedly enhanced with the injection time extension (Supplementary Fig. 24e), which showed the same trend as PA imaging, suggesting the efficient tumor accumulation of Pd_2Sn@GOx-SP. Besides, the real-time temperature change in the tumor site was also monitored by a thermal imaging camera after 6 h of Pd_2Sn@GOx-SP injection. The temperature of the mice tumor raised obviously under the irradiation of laser compared with that without injection of Pd_2Sn@GOx-SP (Supplementary Fig. 24f), exhibiting the superior in vivo photothermal effect of Pd_2Sn@GOx-SP. To sum up, the Pd_2Sn@GOx-SP possessed the potential for PA, CT, and infrared thermal imaging to guide tumor synergistic therapy.

The biosafety and biocompatibility of Pd_2Sn@GOx-SP are prerequisites for in vivo treatment, thus the comprehensive evaluation was performed. To begin with, we examined the hemolysis induction of Pd_2Sn@GOx-SP in red blood cells (Supplementary Fig. 25). The hemolysis assay showed that no significant hemolysis appeared by Pd_2Sn@GOx-SP, even if the concentration reached 500 μg/mL. Moreover, the biodistribution assessment of Pd_2Sn@GOx-SP i.v. injected into CT26-bearing mice was comprehensively analyzed by

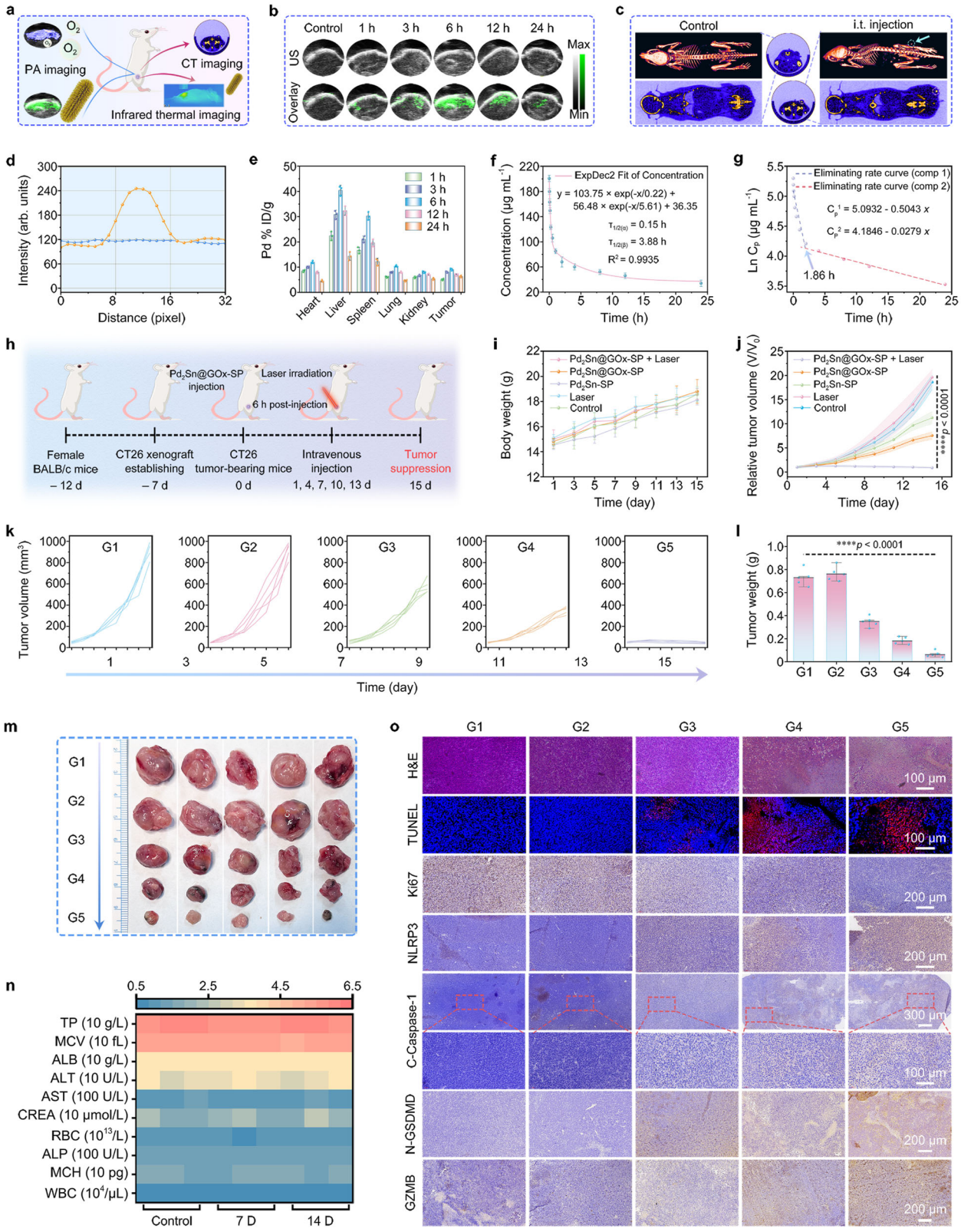

using ICP-OES. As displayed in Fig. 6e, the high contents of Pd were observed in the liver and spleen, which were consistent with the results of ex vivo PA imaging. After 6 h of Pd_2Sn@GOx-SP injection, the Pd levels reached a maximum concentration (9.07% ID g^{-1}) in tumor regions, and maintained a relatively high level (6.33% ID g^{-1}) even at 24 h, demonstrating the superior tumor-homing efficiency of Pd_2Sn@GOx-SP. The high biocompatibility of SP endowed Pd_2Sn@GOx-SP with stable blood circulation capacity. The blood circulation half-life time of Pd_2Sn@GOx-SP was acquired, which was $t_{1/2(\alpha)} = 0.15$ h and $t_{1/2(\beta)} = 3.88$ h (Fig. 6f). Simultaneously, as presented in Fig. 6g, the elimination rate constant of Pd_2Sn@GOx-SP in the first stage was obtained to be −0.5043 μg mL^{-1}/h, which showed a decrease to −0.0279 μg mL^{-1}/h after an interval of 1.86 h. Benefiting from the appropriate blood circulation,

Fig. 6 | In vivo PA/CT imaging-guided synergistic anti-tumor therapy. **a** Schematic illustration of the PA, CT, and infrared thermal imaging. Representative in vivo **b** PA images after being i.v. injected with Pd_2Sn@GOx-SP and **c** CT images after i.t. injected without or with Pd_2Sn@GOx-SP. (one representative data was shown from three independently repeated experiments). **d** The corresponding line profiles of CT values. **e** In vivo biodistribution of Pd_2Sn@GOx-SP in main organs and tumors at various time intervals. Data are expressed as mean ± S.D. ($n = 3$) mice for each group. **f** The blood circulation curve and **g** the eliminating rate curve after i.v. injected with Pd_2Sn@GOx-SP. Data are expressed as mean ± S.D. ($n = 3$) independent animals. **h** Therapeutic schedule of Pd_2Sn@GOx-SP for CT26 tumor-bearing mice. **i** Body weight, **j** relative tumor volume, **k** tumor volume, **l** tumor weight, and **m** the photographs of excised tumors from representative mice in different treatment groups (G1, control; G2, laser; G3, Pd_2Sn-SP; G4, Pd_2Sn@GOx-SP; G5, Pd_2Sn@GOx-SP + laser). Data are expressed as mean ± S.D. ($n = 5$) mice for each group in (**i**, **j**, **l**). **n** Hematological indexes and biochemical data of mice after i.v. injection with PBS and Pd_2Sn@GOx-SP. **o** Staining images of H&E, TUNEL, Ki67, NLRP3, C-Caspase-1, GSDMD, and GZMB for tumor slices from different groups. (one representative data was shown from three independently repeated experiments). Statistical significance is assessed by a two-way ANOVA with Tukey's multiple comparisons test. Source data are provided as a Source Data file (arb. units arbitrary units).

Pd_2Sn@GOx-SP could achieve abundant accumulation in the tumor to exert an anti-tumor effect.

Subsequently, the in vivo anti-cancer efficacy of Pd_2Sn@GOx-SP on CT26-bearing mice was further evaluated (Fig. 6h). Twenty-five female BALB/c mice established with the cancer model were randomly separated into five groups ($n = 5$), containing control (G1), laser (G2), Pd_2Sn-SP (G3), Pd_2Sn@GOx-SP (G4), Pd_2Sn@GOx-SP + laser (G5). All groups were i.v. administered with PBS or nano-drug at a dose of 10 mg kg^{-1}, and irradiated with laser after 6 h of injection. During the treatment process, no significant abnormal body weight fluctuation was displayed in the treated groups (Fig. 6i), indicating high biosafety. As depicted in Fig. 6j, k, control or only laser irradiation resulted in rapid tumor growth, whereas Pd_2Sn-SP alone moderately inhibited tumor growth. Comparatively, the Pd_2Sn@GOx-SP + laser group exerted a significant therapeutic effect with a suppression rate of 83.76% owing to the synergistic effect of pyroptosis with disulfidptosis. Moreover, the tumor weight also exhibited distinct differences after various treatments. The mice in the group of control or only laser possessed heavier tumors while tumor weights of the mice treated with nano-drug were reduced to varying degrees (Fig. 6l). Digital photos of the tumors dissociated from each mouse reflected the identical results (Fig. 6m). After that, the biocompatibility of the Pd_2Sn@GOx-SP was also evaluated by conducting the blood routine and blood biochemical analyses on the treated mice, which could provide the basis for potential practical applications of malignancy treatments. No significant abnormalities were found in the liver and kidney function of the mice before and after i.v. administrated with Pd_2Sn@GOx-SP (Fig. 6n). Moreover, there were also no noticeable changes in hematological biomarkers contrasted with the control group, verifying the insignificant side effects of Pd_2Sn@GOx-SP on hematological system.

To further validate the satisfactory anti-cancer effect of Pd_2Sn@GOx-SP combined with laser, TdT-mediated dUTP nick-end labeling (TUNEL) and hematoxylin–eosin (H&E) staining were proceeded on the slices of tumor tissue collected from the mice with various treatments (Fig. 6o). As expected, the highest degree of cell death was reflected in the group of Pd_2Sn@GOx-SP + laser than the other treatment groups, verifying a favorable tumor therapeutic effect of Pd_2Sn@GOx-SP. Moreover, Ki67 staining was also performed and the group of Pd_2Sn@GOx-SP + laser greatly decreased the expression of Ki67 (Fig. 6o), indicating the prominent inhibition effect for tumor aggressiveness. Furthermore, the underlying therapeutic mechanism induced by Pd_2Sn@GOx-SP via pyroptosis was also confirmed through the immunohistochemical investigation of NLRP3, C-Caspase-1, and GSDMD. All of them were visibly elevated in the tumor tissues extracted from the mice treated with Pd_2Sn@GOx-SP + laser (Fig. 6o), evidencing the occurrence of pyroptosis in tumor cells. Significantly, the main organs of mice with diverse treatments showed no distinct inflammation or pathological changes (Supplementary Fig. 26), which additionally confirmed the remarkable histocompatibility of Pd_2Sn@GOx-SP. Furthermore, we constructed another tumor xenograft model using 4T1 mammary cancer cells to validate the excellent anti-tumor efficacy of Pd_2Sn@GOx-SP (Supplementary Fig. 27a). The results demonstrated that the growth of 4T1 tumors was significantly inhibited by the treatment of Pd_2Sn@GOx-SP + laser (Supplementary Fig. 27b, c). Meanwhile, the body weight of mice in each treatment group exhibited no significant abnormality (Supplementary Fig. 27d), confirming the biosafety of Pd_2Sn@GOx-SP. The excellent tumor suppression effect could also be observed based on the H&E and TUNEL staining images of tumor tissue slices (Supplementary Fig. 27e). Moreover, the H&E staining images of the major organs collected from the mice with diverse treatments showed no distinct inflammatory or pathological changes, which further validated the excellent biosafety of Pd_2Sn@GOx-SP (Supplementary Fig. 27f). These results highlighted the therapeutic potential of Pd_2Sn@GOx-SP, which could induce both pyroptosis and disulfidptosis, making it a promising candidate for treating various types of tumors.

In vivo immune stimulation effect

The release of massive cytoplasmic contents induced by tumor pyroptosis has been demonstrated to trigger immune responses for achieving anti-tumor immune activity and cancer immunotherapy (Fig. 7a)[25]. The reconstruction of the immunosuppressive microenvironment elicited by Pd_2Sn@GOx-SP was investigated by flow cytometry analysis. Similar to the in vitro experimental results, the Pd_2Sn@GOx-SP + laser group induced a higher proportion of DCs maturation in spleens than that of other groups (Fig. 7b, c). The mature DCs play an important role in antigen presentation, thereby activating the proliferation of naive T cells and evoking an adaptive immune response[44,55]. To further confirm the immunotherapeutic effect of Pd_2Sn@GOx-SP, the spleen infiltrating T cells were emphatically evaluated. As unfolded in Fig. 7d, e, the proportions of $CD4^+$ and $CD8^+$ T cells in Pd_2Sn@GOx-SP + laser group could reach 47.0% and 37.7%, which were over 1.9 and 4.4 folds more than those in the control group, respectively. Importantly, the IFN-γ levels distinctly elevated in the tumors of the mice treated with Pd_2Sn@GOx-SP + laser, which was 6.5 folds higher than the mice in control group (Fig. 7f, g), demonstrating the effective activation of $CD8^+$ T cells[56].

Simultaneously, the activation of T cells in tumors was also analyzed (Supplementary Fig. 28a). The counts of $CD8^+$ T cells in the group of Pd_2Sn@GOx-SP + laser increased by 4.3 folds than that in control group (Fig. 7h). Moreover, the expression level of granzyme B (GZMB) in $CD8^+$ T cells is also a good marker of anti-cancer immunity activation. The expression level of GZMB in tumors was evaluated by immunohistochemical analysis to confirm the activation of anti-cancer immunity. As can be seen in Fig. 6o, the GZMB levels were significantly upregulated in the tumors of the mice treated with Pd_2Sn@GOx-SP + laser compared with other groups, demonstrating the effective activation of $CD8^+$ T cells to achieve anti-cancer immunity. Tumor-associated macrophages (TAMs) are the prominent immune cells present in the tumor stroma[57,58]. The activated macrophages mainly comprise M1-type and M2-type, which show pro-inflammatory and anti-inflammatory properties, respectively. M2-type TAMs usually endow TME with characteristics of immunosuppression, promoting the progression of tumor[59,60]. Consequently, the repolarization of M2-type TAMs to M1-type TAMs could reverse the tumor

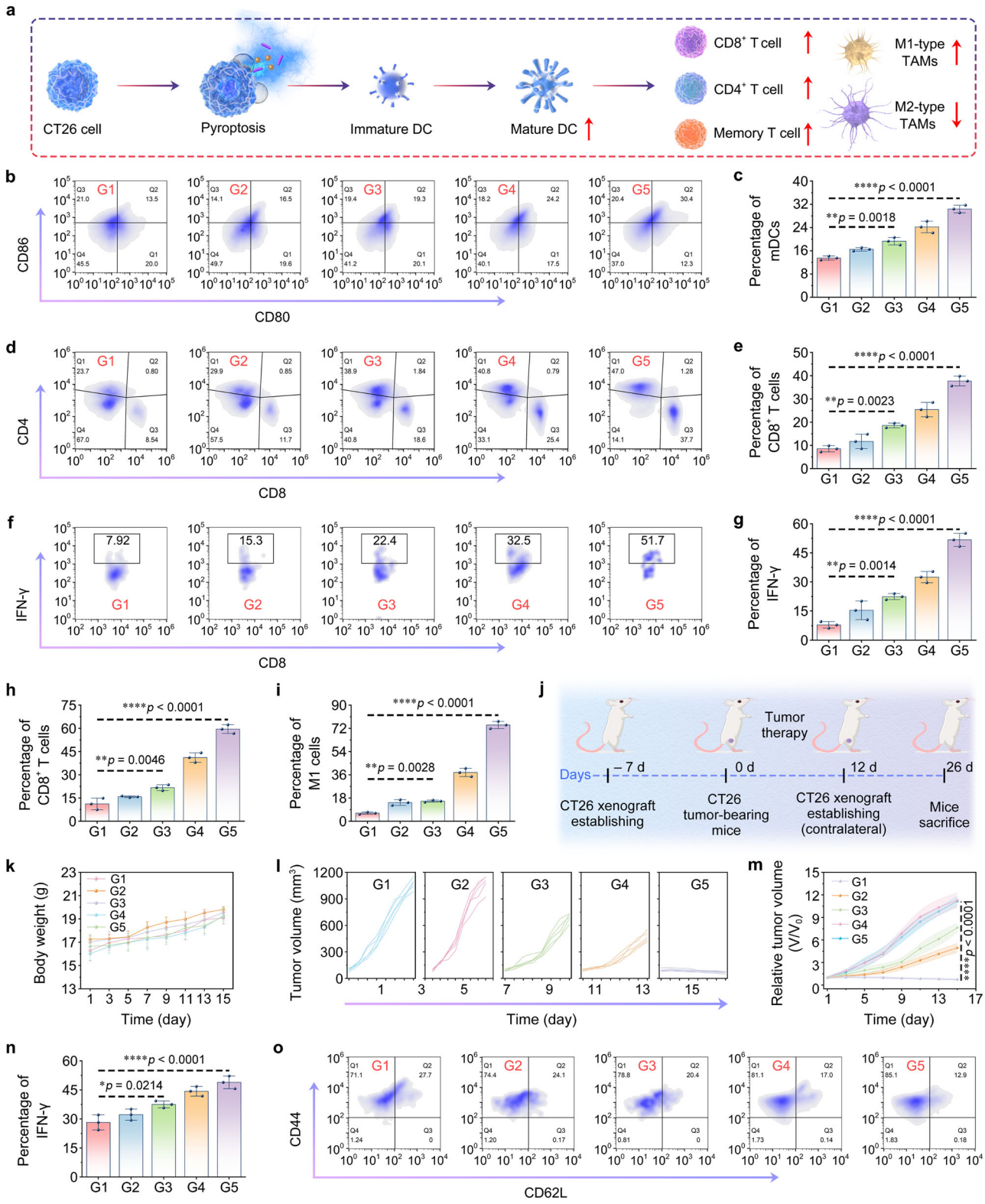

immunosuppression, which is beneficial for tumor therapeutic effect[61,62]. Consequently, the capability of Pd_2Sn@GOx-SP to alter the phenotype of TAMs was explored in mouse tumors (Supplementary Fig. 28b). M2-type TAMs obviously decreased in the Pd_2Sn@GOx-SP + laser group than that in control group, while the ratio of M1-type TAMs raised from 6.23% to 74.6% (Fig. 7i), indicating the laser-amplified and excellent tumor immunotherapy effect of Pd_2Sn@GOx-SP. All these data provide convincing evidence that the Pd_2Sn@GOx-SP could recruit immune cells into tumors to induce specific anti-tumor immunity.

Tumor immunotherapy could stimulate the immune system to derive a long-term anti-tumor immunological response, which could prevent the recurrence and metastasis of tumors[63]. Encouraged by the excellent activation of immunity and treatment effect on the primary tumor, we further investigated the efficacy of Pd_2Sn@GOx-SP on mouse models with recurrence by a tumor-challenging assay (Fig. 7j).

Fig. 7 | In vivo immune stimulation effect of Pd_2Sn@GOx-SP. a Pattern diagram for remodeling the immunosuppressive TME. **b** Representative flow cytometry data and **c** the quantitative data of matured DCs in spleens after receiving diverse treatments (G1, control; G2, laser; G3, Pd_2Sn-SP; G4, Pd_2Sn@GOx-SP; G5, Pd_2Sn@GOx-SP + laser). **d** Representative flow cytometry data and **e** the quantitative data of $CD8^+$ T cells in spleens after receiving diverse treatments. **f** Representative flow cytometry data and **g** the quantitative data of IFN-γ level in tumor tissues after diverse treatments. **h** The corresponding quantitative data of $CD8^+$ T cells in tumor tissues after receiving different treatments. **i** The corresponding quantitative data of M1-type macrophages ($CD86^+$ and $CD206^-$ cells) in tumor. **j** Schematic diagram of the schedule for tumor rechallenge study. **k** Body weight changes of CT26 recurrence tumor-bearing mice with diverse treatments. **l** Tumor volume and **m** relative tumor volume of recurrence tumor in CT26 tumor-bearing mice with diverse treatments. **n** The corresponding quantitative data of IFN-γ level in recurrence tumor tissues. **o** Representative flow cytometry data of T_{EM} ($CD62L^-$ and $CD44^+$ cells) in spleens after receiving diverse treatments. Data are expressed as mean ± S.D. ($n = 3$) independent samples in (**c**, **e**, **g**–**i**, **n**), ($n = 5$) mice for each group in (**k**, **m**). Statistical significance is assessed by a two-way ANOVA with Tukey's multiple comparisons test. Source data are provided as a Source Data file.

The body weights and rechallenge tumor volumes of all the mice with various treatments were measured during the treatment process (Fig. 7k, l). The rechallenge tumors in the Pd_2Sn@GOx-SP + laser group were the smallest among all the groups (Fig. 7m), indicating that the immune memory induced by Pd_2Sn@GOx-SP could effectively inhibit tumor recurrence. Subsequently, the immune mechanism of the distal tumor tissues in various groups was further investigated. As depicted in Supplementary Fig. 29a, the ratio of $CD8^+$ T cells in the distant tumors was increased to 17.3 after treatment with Pd_2Sn@GOx-SP + laser, which was over 5.3 folds higher than that in control group. Simultaneously, the IFN-γ levels in distant tumors were also evaluated (Supplementary Fig. 29b). Results indicated that the secretion of IFN-γ significantly increased in the Pd_2Sn@GOx-SP treated group (Fig. 7n), which was beneficial to the subsequent activation of anti-tumor immunity. Furthermore, depleting antibodies against CD8 (anti-CD8α) were injected into mice to deplete $CD8^+$ T cells, and the tumor growth was monitored to confirm that the treatment involves the activation of anti-cancer immunity (Supplementary Fig. 27a). After the depletion of $CD8^+$ T cells by the administration of anti-CD8α, the therapeutic efficacy of Pd_2Sn@GOx-SP + laser decreased significantly (Supplementary Fig. 27g). All these data provide convincing evidence that Pd_2Sn@GOx-SP could recruit immune cells to tumors, thereby inducing a specific anti-tumor immune response.

Motivated by satisfactory immune response of Pd_2Sn@GOx-SP, the activation of immune memory was further evaluated by analyzing the proportion of effector memory T cells (T_{EM}, $CD62L^-CD44^+$) and central memory T cells (T_{CM}, $CD62L^+CD44^+$) in spleens (Fig. 7o). The ratios of T_{EM} in the group of Pd_2Sn@GOx-SP + laser increased to 85.1%, which was higher than that in control group, indicating a potent immune memory was formed. These results demonstrated that Pd_2Sn@GOx-SP could effectively reshape the immunosuppressive TME and stimulate the intense immune response, thereby effectively expunging dormant tumor cells and hindering their recurrence. After that, the inhibitory effects of Pd_2Sn@GOx-SP on lung metastasis were further investigated by establishing a pulmonary metastasis model to confirm the immune memory effect (Supplementary Fig. 30a). After all the treatments, the CT26-bearing mice were i.v. injected with CT26 cells to imitate lung metastasis, and the lungs of the mice were harvested after 13 days. The photographs and H&E staining images of lung tissues showed that abundant nodules in the lung collected from the control group, and a significant improvement was observed in the Pd_2Sn@GOx-SP group, but there was no obvious metastasis in the Pd_2Sn@GOx-SP + laser combined treatment group (Supplementary Fig. 30b). In general, the Pd_2Sn@GOx-SP with satisfactory biosecurity could promote the maturation and infiltration of cytotoxic T lymphocytes, which activated strong systematic immune responses against tumor recurrence and metastasis. Therefore, the Pd_2Sn@GOx-SP-mediated pyroptosis and disulfidptosis could effectively inhibit tumor growth, recurrence, and spontaneous metastases.

RNA-sequencing analysis of anti-cancer mechanism

Given the effective therapeutic effect and immune activation of Pd_2Sn@GOx-SP on tumors, we further explored the potential therapeutic mechanism by analyzing the mRNA profiles through high-throughput RNA sequencing. In total, 964 differentially expressed genes (DEGs) were screened out between the Pd_2Sn@GOx-SP + laser and control groups, of which 602 (62.45%) genes were upregulated and 362 (37.55%) genes were downregulated (Fig. 8a–c). Subsequently, the Kyoto Encyclopedia of Genes and Genomes (KEGG) and Gene Ontology (GO) analysis of DEGs was conducted to examine the biological roles (Fig. 8d, e). The results suggested that the DEGs correlated with Pd_2Sn@GOx-SP + laser treatment were related to immunity pathways, demonstrating that Pd_2Sn@GOx-SP + laser could activate the immune response by triggering programmed death of tumor cells. This discovery highlights the importance of these genes in immune regulation, providing important clues for us to understand their potential roles in diseases or biological processes. In addition, the correlation between the downregulated genes and cell adhesion was confirmed by the GO enrichment analysis, which is critical for cell migration, further confirming the inhibition of tumor cell migration by the Pd_2Sn@GOx-SP + laser treatment. Furthermore, gene set enrichment analysis (GSEA) confirmed that the DEGs were involved in pathways associated with pyroptosis (Fig. 8f). Additionally, heat maps of DEGs associated with disulfidptosis were also generated (Fig. 8g). The expression of disulfidptosis-related genes (including NDUFA11, GYS1, OXSM, LRPPRC, NDUFS1, NCKAP1, PRDX1, RPN1, and NUBPL) was notably upregulated in the Pd_2Sn@GOx-SP + laser treatment group[9]. The evident genetic changes demonstrated that Pd_2Sn@GOx-SP + laser could induce tumor cell death via pyroptosis and disulfidptosis processes.

Discussion

In summary, the precise pyroptosis and disulfidptosis dual-inducer of intermetallic Pd_2Sn modified with GOx was developed for exerting anti-tumor immune effects. Various morphologies (including NDs and NRs with different lengths) of Pd_2Sn intermetallic compounds were constructed and the properties were further contrasted. Both in vitro experiments and DFT calculations results confirmed that the NRs with the highest specific surface area exhibit the best catalytic performance. The intermetallic Pd_2Sn with ordered structure displayed enhanced NIR light absorption and multiple enzyme catalytic activities (CAT, POD, and OXD-mimic activity), which facilitate photothermal conversion and ROS generation, thereby achieving GSDMD-dependent pyroptosis. Additionally, owing to the consumption of glucose by integrated GOx, Pd_2Sn@GOx-SP could increase the $NADP^+$/NADPH ratio, leading to the abundant accumulation of cystine in CT26 cells with high SLC7A11 expression, achieving cystine-related disulfidptosis. Moreover, the enhanced cascade catalytic reaction could also be realized by the generation of H_2O_2, photothermal effect, production of O_2, and GSH depletion triggered by the complementary relationship of Pd_2Sn and GOx. Notably, Pd_2Sn@GOx-SP-induced pyroptosis and disulfidptosis could effectively reprogram TME by alleviating immunosuppression and promoting T cell infiltration, thus promoting immune responses mediated by T cells, which are conducive to the inhibition of tumor metastasis and recurrence. This work not only provided a strategy for the imaging-guided dual-inducer design of pyroptosis and disulfidptosis, but also broadened the biomedical

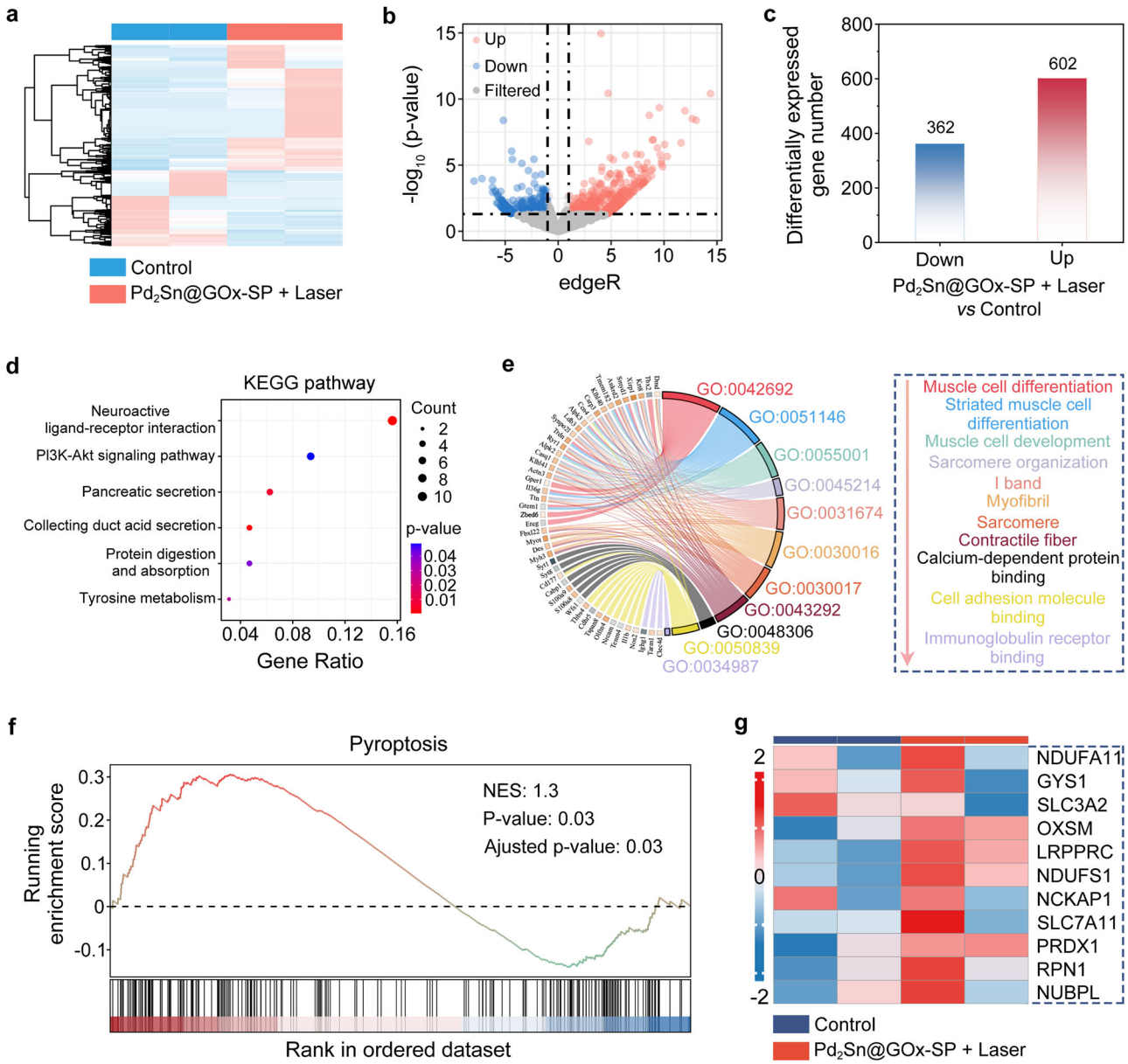

Fig. 8 | Transcriptional analysis of anti-tumor mechanism induced by Pd_2Sn@GOx-SP. a Cluster diagram of DEGs between Pd_2Sn@GOx-SP + laser and control groups. **b** Volcano plots and **c** numbers of the upregulated and down-regulated genes of Pd_2Sn@GOx-SP + laser groups compared with control groups. Statistical significance is assessed by two-sided *t*-test. **d** KEGG pathway enrichment analysis. **e** The circle diagram of GO enrichment analysis. Statistical significance is assessed by one-sided *t*-test. **f** GSEA of pyroptosis signaling pathway. Statistical significance is assessed by one-sided *t*-test. **g** Cluster heatmap of the DEGs associated with disulfidptosis between Pd_2Sn@GOx-SP + laser and control groups. Source data are provided as a Source Data file ($n = 3$ mice).

applications of intermetallic compounds, which offers good prospects for future advancement of cancer immunotherapy.

Methods

Animal care

Female BALB/c mice (4-week-old) were obtained from Beijing Vital River Laboratory Animal Technology Co., Ltd. (Beijing, China) (1100111084356). The animal experiments were conducted with the approval of ethics by the Ethics Committee of Harbin Medical University Cancer Hospital (No. KY2024-33). Experimental group sizes were approved by the Regulatory Authorities for Animal Welfare after being defined to balance statistical power, feasibility, and ethical aspects. CT26 cells or 4T1 cells (1×10^6, 100 μL in PBS) were subcutaneously injected into the right back of each BALB/c mouse when they were 5 weeks old to establish CT26 or 4T1 tumor models, and the following experiments were conducted when the tumor volume approached 60 mm^3. The maximal tumor size/burden permitted by the ethics committee is 1500 mm^3, and the maximal tumor size/burden was not exceeded in the experiments. The sex of the animal was not specifically considered in this study. Mice of the appropriate sex were employed according to the requirements of the tumor model. A female mouse model was employed for CT26 colon cancer and 4T1 breast cancer. Mice were housed in a specific-pathogen-free condition at 26 ± 1 °C and 50 ± 5% humidity with a 12-h light–dark cycle with unrestricted access to food and water.

Chemicals and materials

Oleylamine, MAHC, $Pd(acac)_2$, $Sn(OAc)_2$, TOP, GOx, SP, TMB, MB, DMPO, and OPD were purchased from Sigma-Aldrich (Shanghai, China). Ethanol and chloroform were of analytical grade and

purchased from various sources. MTT, DCFH-DA, 4′,6-diamidino-2-phenylindole (DAPI), Calcein-AM and propidium iodide (PI), JC-1 staining kit, and ActinGreen were purchased from Beyotime Inst. Biotech. (Haimen, China). $[Ru(dpp)_3]Cl_2$ (cat: MX4826) was purchased from MKBIO (Shanghai, China). Anti-CRT (AF1666) and anti-HMGB1 (PH406) were purchased from Beyotime. ATP content assay kit was obtained from Shanghai EnzymeLink Biotechnology Co., Ltd. (Shanghai China). The glutathione assay kit and glucose assay kit were purchased from Wanleibio Co., Ltd. Anti-Granzyme B (ab4059) was obtained from Abcam. Filamin A Rabbit pAb (A0927) was purchased from Company ABclonal, Inc. MYH9 Polyclonal antibody (cat. 11128-1-AP) and Talin-1 Polyclonal antibody (cat. 14168-1-AP) were purchased from Proteintech Group, Inc. Ferrostatin-1 and Erastin were obtained from MedChemExpress. DTT, RPMI 1640 medium, fetal bovine serum (FBS), and Dulbecco's modified Eagle medium (DMEM) were purchased from Thermo Fisher Scientific Inc. Anti-CD45-APC/Cyanine7 (cat.103116), anti-CD3-PerCP/Cyanine5.5 (cat.100218), anti-CD4-FITC (cat.100406), anti-CD8a-APC (cat.100712), anti-CD11c-FITC (cat.117306), anti-CD86-APC (cat.105012), anti-CD80-PE (cat.104708), anti-CD11b-FITC (cat.101206), anti-F4/80-PerCP/Cyanine5.5 (cat.123126), anti-CD206-PE (cat.141706), anti-CD44-FITC (cat.103022), anti-CD62L-PE (cat.161204), anti-IFN-γ-PE (cat.505808) were purchased from Biolegend (USA). InVivoMAb anti-mouse CD8α (cat. BE0061) was purchased from BioXCell. H&E Stain Kit was obtained from Beijing Solarbio Science & Technology Co., Ltd. (Beijing, China). The TUNEL cell apoptosis detection kit was bought from Dalian Meilun Biotechnology Co., Ltd. All chemicals were used as received without further treatment.

Characterization

The PXRD measurement was examined with a Rigaku D/max-TTR-III diffractometer using Cu-Ka radiation (λ = 0.15405 nm) at 40 kV and 40 mA. TEM and HRTEM were recorded on an FEI Tecnai G2 S-Twin transmission electron microscope equipped with a field emission gun operating at 200 kV. XPS spectra were carried out using an ESCALAB 250 instrument. The zeta potential measurement for different samples was performed on a Malvern Zeta sizer Nan Nano ZS90. A UV-1601 spectrophotometer was used to obtain the UV–vis–NIR absorption spectrum. ESR spectra were acquired by a Bruker EMX1598 spectrometer. The element quantitative analysis of the sample was conducted on ICP-OES (Agilent 725, Agilent Technologies, USA). The flow cytometry assays were performed on a BD Accuri C6 flow cytometer (USA). A CLSM (Leica TCS SP8) was adopted to obtain the fluorescence image.

Synthesis of Pd_2Sn

The Pd_2Sn with different morphology were synthesized with the same procedure, except for the amount of MAHC added. Briefly, oleylamine (20 mL), a certain quantity of MAHC, $Pd(acac)_2$ (0.2 mmol), and $Sn(OAc)_2$ (0.1 mmol) were added into the four-necked flask (100 mL). Under continuous stirring at 40 °C, the flask containing various precursors was vacuumed for 20 min, then protected by injecting with nitrogen at 60 °C for 30 min to form a uniform solution. After that, the TOP (1 mL) was injected into a four-necked flask and quickly heated up to 200 °C and maintained at this temperature for 30 min. Subsequently, the mixed solution in the flask was heated to 300 °C and preserved for another 30 min. Finally, the flask was discontinued heating and cooled to room temperature (RT) naturally. Pd_2Sn intermetallics were obtained by centrifugation and washed with ethanol and chloroform. In a controllable way, the Pd_2Sn NDs or NRs with different lengths were synthesized by adding MAHC with different amounts.

Synthesis of Pd_2Sn@GOx-SP

The as-prepared Pd_2Sn nanoparticles dissolved in cyclohexane (1 mg mL^{-1}, 10 mL) were added dropwise into chloroform solution of SP (2 mg mL^{-1}, 30 mL). The solvent of the mixture was evaporated in a rotary evaporator under a vacuum at 60 °C to collect Pd_2Sn-SP. Then, the obtained Pd_2Sn-SP and GOx (5 mg) were dispersed in H_2O and stirred vigorously overnight. The Pd_2Sn@GOx-SP nanocomposites were performed by centrifugation and washed with water and ethanol for further use.

In vitro photothermal performance of Pd_2Sn-SP

The laser wavelength used in this work was 808 nm, which was generated by the 808 nm multimode fiber coupled laser (Changchun Laser Optoelectronics Technology Co., Ltd). The power density of the 808 nm laser used in the in vitro or in vivo experiments was 0.8 W cm^{-2}. The rod-shaped Pd_2Sn-SP solution with various concentrations was irradiated with laser at RT for 10 min and photographed at specified intervals by thermal imaging equipment (FLIR System E40). In addition, pure water was performed as a comparison. Furthermore, the Pd_2Sn-SP solution was irradiated with a laser for four cycles to explore the photothermal stability, and the change of temperature was plotted. Selecting the cooling phase curve to calculate the photothermal conversion efficiency (η) of Pd_2Sn-SP based on the following formula:

$$\eta = \frac{hA(T_{max} - T_{surr}) - Q_s}{I(1 - 10^{-A_\lambda})} \quad (1)$$

h, A, T_{max}, T_{surr}, I, and A_λ refer to heat transfer coefficient, superficial area, maximum equilibrium temperature, ambient temperature, laser fluence, and absorption value, respectively. $Q_s = (5.4 \times 10^{-4})\ I$.

ESR measurement

The ·OH was measured by using DMPO as the trapping agent through ESR analysis. The Pd_2Sn-SP (100 μL, 1 mg mL^{-1}), PBS (340 μL, pH = 5.5), and DMPO (10 μL) were mixed, and the solution was analyzed by an electron paramagnetic resonance spectrometer after the rapid injection of H_2O_2 (100 mM, 50 μL). In addition, the stimulation of the laser was performed at the same reaction time, and the characteristic signal peak with the intensity of 1:2:2:1 for ·OH was captured.

Catalase (CAT)-mimic activity of Pd_2Sn-SP

The detection of O_2 generation induced by Pd_2Sn-SP with different morphologies was conducted to evaluate the CAT-mimic activity by using a dissolved oxygen meter. In a typical process, the Pd_2Sn-SP (0, 50, 100, 200, and 400 μg mL^{-1}) was mixed with H_2O_2, and the oxygen concentration (mg L^{-1}) was recorded last for 6 min, respectively.

Oxidase (OXD)-mimic activity of Pd_2Sn-SP

TMB as the substrate was used to measure the OXD-mimic activity of Pd_2Sn-SP. Typically, TMB (300 μg mL^{-1}) and Pd_2Sn-SP (200 μg mL^{-1}) were dispersed in PBS (3 mL) at RT, and the absorbance was measured after a certain reaction time by using a UV–vis–NIR spectrophotometer.

Glucose consumption

Pd_2Sn@GOx-SP (0 and 200 μg mL^{-1}) were mixed with glucose solution (1 mg mL^{-1}). At various time intervals, the mixed solution (0.5 mL) was added with dinitrosalicylic acid (DNS) reagent (1.5 mL). Then, the mixed solution was heated to 100 °C and maintained for 5 min, then cooled to RT. Subsequently, the absorbance of the mixed solution at 595 nm was measured by UV–vis–NIR spectrophotometer.

Peroxidase (POD)-mimic activity of Pd_2Sn-SP and kinetic assay

The POD-mimic activity for the ·OH generation of Pd_2Sn-SP was measured using TMB and OPD as the substrates. Briefly, 3 mL PBS including Pd_2Sn-SP (100 μg mL^{-1}) and TMB (300 μg mL^{-1}) was mixed with H_2O_2, and the absorbance in various groups was recorded after a certain

reaction time. The groups exposed to a laser were performed at the same conditions except for laser action.

The POD-mimicking kinetics of Pd_2Sn-SP (NDs, short NRs, medium NRs, long NRs) with different morphologies were also evaluated. TMB (300 μg mL^{-1}), Pd_2Sn-SP (100 μg mL^{-1}), and H_2O_2 (final concentrations of 1, 2, 4, 8, and 16 mM) were mixed in PBS (3 mL) at RT, the absorbance intensity at 652 nm were measured on a UV–vis–NIR spectrophotometer, and the Michaelis–Menten equation was adopted to analyze the Michaelis–Menten constant.

The catalytic activity of Pd_2Sn-SP with different morphologies was further evaluated by altering the amounts of Pd_2Sn-SP. Similarly, equivalent TMB, H_2O_2, and different amounts of Pd_2Sn-SP were added into PBS (3 mL) at RT, and the absorbance of the mixed solution was recorded at various times. The catalytic activity (units) was calculated to make a comparison of the Pd_2Sn-SP with different morphologies.

MB degradation assay

The prepared MB aqueous solution (10 μg mL^{-1}) was mixed with Pd_2Sn-SP to form a mixed solution uniformly, which was injected into the H_2O_2 solution (final concentration of 50 μM) rapidly. The absorbance of the mixed solution was detected at various time intervals.

DPA degradation assay

The generation of singlet oxygen ($^1O_2$) by Pd_2Sn-SP was measured using DPA as the substrate. First, DPA (1 mg mL^{-1}) was dissolved in DMSO and mixed with Pd_2Sn-SP. Then, an 808 nm laser was used to irradiate the mixture, the absorbance was measured at various times.

Density functional theory (DFT) calculation

The Vienna Ab initio Simulation Package was used for DFT calculation. The plane wave cutoff was set to 500 eV, and the integration over the Brillouin zone was treated by the Monkhorst–Pack technique with a $(2 \times 2 \times 1)$ grid for relevant surfaces and a $(4 \times 4 \times 4)$ one for the bulk crystal. The energy and force are converged when the values are $<1 \times 10^{-5}$ eV and −0.05 eV/Å, respectively. For bulk crystal, a $(2 \times 2 \times 1)$ supercell containing 24 atoms was considered, while the $(2 \times 2 \times 1)$ supercell for the relevant Pd_2Sn (001, 010, 011) surfaces was used. The (001, 010, 011) surfaces of different models were employed in the whole calculation process owing to the (001, 010, 011) crystal planes are the main exposed crystal planes.

Cell culture

The L929, 3T3, CT26, 4T1, HeLa, SW1990, A549, and HepG2 cells were obtained from the Heilongjiang Key Laboratory of Molecular Oncology. The L929, HeLa, and HepG2 cells were seeded in minimum Eagle's medium (Procell, Wuhan, China), 3T3 cells were seeded in DMEM (Procell, Wuhan, China), CT26 and 4T1 cells were seeded in RPMI 1640 medium (Procell, Wuhan, China), SW1990 cells were seeded in Leibovitz's L-15 medium (Procell, Wuhan, China), A549 cells were seeded in Ham's F-12K medium (Procell, Wuhan, China), and all medium were added with 10% FBS and 1% penicillin–streptomycin. The cells were cultured at 37 °C under a 5% CO_2 atmosphere.

Cellular uptake and subcellular localization

CT26 cells were seeded in 6-well plates and cultured for 24 h. Then, the cell culture medium was replaced with a fresh culture medium containing FITC-labeled Pd_2Sn@GOx-SP for 0, 1, 2, 4, and 8 h, respectively. For subcellular localization, the treated cells were further stained with commercial Lyso-Tracker Red DND-99 (100 nM) and DAPI according to the manufacturer's guidelines. The fluorescence images of cells were captured by CLSM after rinsing with PBS and fixing with glutaraldehyde (2.5%). The colocalization analysis was performed by Image J software. For the flow cytometry assay, the treated cells were resuspended by trypsin and washed with PBS, and the fluorescence intensity of the cells was recorded by a flow cytometer.

In vitro cytotoxicity assay

L929, 3T3, and CT26 cells were cultured in 96-well plates for 12 h. Then, the cell culture medium was refreshed with a fresh culture medium containing Pd_2Sn-SP or Pd_2Sn@GOx-SP with different concentrations, and the laser-related groups were irradiated with an 808 nm laser. Finally, the standard MTT assay was conducted. Similarly, 4T1, HeLa, SW1990, A549, and HepG2 cells were cultured in 96-well plates for 12 h. Then, these cells were treated with Pd_2Sn@GOx-SP + laser, and the relative cell viability was obtained by MTT assay.

In vitro cell experiments evaluation

For most cell experiments, CT26 cells are subjected to the same culture and subsequent processing. Briefly, CT26 cells were seeded in a 6-well plate and cultured for 24 h. Then, the cultivated cells were performed with different conditions, containing control (G1), laser (G2), Pd_2Sn-SP (G3), Pd_2Sn@GOx-SP (G4), Pd_2Sn@GOx-SP + laser (G5). After co-incubation at 37 °C for 4 h, the laser-related groups were irradiated with 808 nm laser (0.8 W cm^{-2}, 5 min), and then the cells were stained with the corresponding fluorescent dyes for analysis.

For the detection of intracellular ROS production, the treated cells were stained with DCFH-DA and DAPI for 20 and 15 min in the dark, respectively. Finally, the fluorescence of cells was captured by a CLSM. For flow cytometry analysis, the treated cells were resuspended by trypsin and washed with PBS, and the fluorescence intensity of the cells was recorded by a flow cytometer.

For the detection of intracellular O_2 generation, the cells were treated with $[Ru(dpp)_3]Cl_2$ (with the final concentration of 30 μM) for 6 h before various treatments. The treated cells were stained with DAPI for 15 min. Finally, the fluorescence of cells was observed by a CLSM.

For the detection of mitochondrial membrane potential, the treated cells were stained with JC-1 and DAPI for 20 and 15 min, respectively. Finally, the fluorescence of cells was detected by a CLSM.

For the detection of living/dead cells, the treated cells were stained with Calcein-AM and PI at 37 °C for 30 min. Finally, the fluorescence of cells was captured by a CLSM. For the cell death analysis, the treated cells were stained with Annexin V-FITC/PI apoptosis detection kit. Finally, the cells were detected by a flow cytometer.

For the observation of cell morphology, the morphology of the treated cells was directly observed by a fluorescence microscope. Furthermore, the treated CT26 cells were treated with trypsin and then centrifuged to collect the precipitate, which was fixed, dehydrated, embedded, sliced, and measured by bio-TEM.

For the CRT exposure and HMGB1 migration analysis, the treated CT26 cells were washed with PBS and fixed with stationary liquid for 10 min. The anti-CRT and anti-HMGB1 were added to the cells and incubated at 4 °C for overnight, respectively. Finally, the cells were further incubated by Alexa Fluor 488 or Alexa Fluor 555-conjugated secondary antibody and DAPI. Finally, the fluorescence of cells was captured by a CLSM.

In vitro tumor spheroid assay

CT26 cells were cultured in a 96-well plate coated with 1.5% agarose and monitored until the spheroid size reached about 600 μm. Then, fresh culture medium containing FITC-labeled Pd_2Sn@GOx-SP was adopted to replace the old culture medium and co-cultured for 0, 2, 4, and 8 h, respectively. Finally, the tumor spheroids were cleaned with PBS and the fluorescence intensity was observed by a CLSM.

For the cytotoxicity analysis of Pd_2Sn@GOx-SP on tumor spheroids, the tumor spheroids were performed with different conditions (G1, control; G2, laser; G3, Pd_2Sn-SP; G4, Pd_2Sn@GOx-SP; G5, Pd_2Sn@GOx-SP + laser). After co-incubation at 37 °C for 8 h, the laser-related groups were exposed to laser, and then the tumor spheroids were stained with Calcein-AM and PI for 30 min. Finally, the fluorescence of cells was captured by a CLSM.

GSDMD and NLRP3 knockdown

GSDMD and NLRP3 siRNAs obtained from General Biology (Anhui, China) were transfected into CT26 cells. The siRNA sequences of GSDMD were (5′-CCGAGGUGCUGCAGACAAATT-3′) and (5′-UUUGUC UGCAGCACCUCGGTT-3′), (5′-CCUCAGAACUGGAGAGCUUTT-3′) and (5′-AAGCUCUCCAGUUCUGAGGTT-3′), (5′-GCUAGAAGAAUGUGGCCU ATT-3′) and (5′-UAGGCCACAUUCUUCUAGCTT-3′). The siRNA sequences for NLRP3 were (5′-GAAAGAAACUGCUGCCCAATT-3′) and (5′-UUGGGCAGCAGUUUCUUUCTT-3′), (5′-GUACUUAAAUCGUGAAA-CATT-3′) and (5′-UGUUUCACGAUUUAAGUACTT-3′), (5′-GGAUGGGU UUGCUGGGAUATT-3′) and (5′-UAUCCCAGCAAACCCAUCCTT-3′). Empty planter plasmid or siRNA control plasmid was used as a negative control. Briefly, CT26 cells were grown in 6-well plates and transformed with 2 μg of plasmids using Lipofectamine 2000 (Invitrogen, Waltham, MA, USA) according to the manufacturer's protocol. After the transformation of 48 h, cells were harvested for further experiments. The effectiveness of knockdown was confirmed by using western blot.

Western blotting

CT26 cells were seeded in a 6-well plate and cultured for 24 h. The cultivated cells were performed with different conditions (G1–G5). Then, the cells were washed with cold PBS for twice and added to ice-cold lysis buffer for western blotting (Beyotime, China). Protein concentration was determined using the BCA protein assay kit (Beyotime, China). The protein with the same amount was added to a 10% SDS polyacrylamide gel, electrophoresed, and transferred to polyvinylidene fluoride (PVDF) membranes (Roche Diagnostics GmbH, Mannheim, Germany). Then, 5% skimmed milk was used to block the gels for 1 h, which were further incubated with primary antibodies and secondary antibodies. Finally, the protein bands were detected with a fluorescent luminescence detector. The antibodies used in this study were as follows: NLRP3 (15101, CST), anti-GSDMD antibody (69469, CST), anti-Caspase-1 antibody (3866, CST), anti-β-actin antibody (TA-09, ZSGB-BIO), anti-GSDMD-N (69469, CST), and SLC7A11 (PK30003, Proteintech).

In vitro dendritic cells (DCs) stimulation

The bone-marrow-derived DCs were obtained from the leg bones of male BALB/c mice. To begin with, the cultured CT26 cells were performed with different treatments (G1–G5). Then, the treated CT26 cells were collected and co-cultured with immature DCs for 24 h. Finally, the non-adherent cells were collected and stained with anti-CD11c-FITC, anti-CD86-APC, and anti-CD80-PE antibodies to analyze the maturation level of DCs by flow cytometry.

In vitro and in vivo PA and CT imaging performance

Pd_2Sn-SP with various concentrations were prepared to explore the in vitro imaging performance by the PA and CT equipment. As for the in vivo PA and CT imaging, the Pd_2Sn-SP (100 μL) dissolved in saline was i.v. administrated into tumor-bearing mice (at the dose of 10 mg kg^{-1}). In addition, the Pd_2Sn-SP (100 μL) dissolved in saline was also i.t. injected into tumor-bearing mice to further investigate the CT imaging effect. The PA and CT imaging was obtained at various times by using a Vevo LAZR system (VisualSonics Inc. New York, NY) and a small animal X-ray CT imaging system (Quantum GX, PerkinElmer), respectively. In addition, the blood oxygen saturation (SaO_2) in the tumor was further monitored at various times.

In vivo biodistribution and pharmacokinetics of Pd_2Sn@GOx-SP

The tumor-bearing mice ($n = 3$ mice for each group) were treated by i.v. injection with Pd_2Sn@GOx-SP (at the dose of 10 mg kg^{-1}). After 1, 3, 6, 12, and 24 h, the major organs and tumors were collected by sacrificing these mice and analyzed by an ICP-OES. For pharmacokinetics analysis, the BALB/c mice ($n = 3$ mice for each group) were treated by i.v. injection with Pd_2Sn@GOx-SP (at the dose of 10 mg kg^{-1}). After 0, 2, 4, 8, 15, 30 min, 1, 2, 4, 8, 12, and 24 h, the blood was extracted and analyzed by an ICP-OES.

In vivo therapeutic evaluation of Pd_2Sn@GOx-SP

The tumor-bearing mice were randomly allocated into five groups ($n = 5$ mice for each group), including control (G1), laser (G2), Pd_2Sn-SP (G3), Pd_2Sn@GOx-SP (G4), Pd_2Sn@GOx-SP + laser (G5). The mice were i.v. injected with saline or nano-drug on days 1, 5, 9, and 13. During the treatment process, the body weight and tumor size of the mice were measured every 2 days. The tumor volume (V) was calculated according to $V = lw^2/2$. The mice were sacrificed on day 15, and the tumors and main organs were collected for further analysis. The tumor sections of different groups were stained with H&E, TUNEL, Ki67, C-Caspase-1, and NLRP3. The main organ sections were stained with H&E.

To conduct the tumor rechallenge assay, the tumor-bearing mice were randomly allocated into five groups (G1–G5, $n = 5$ mice for each group). On day 12, the mice were rechallenged with CT26 cells (1×10^6) on the left back. The body weight and tumor size were measured every 2 days. On day 26, the mice were sacrificed and the spleens were collected to detect immune cells.

To explore the in vivo anti-metastasis efficacy, the tumor-bearing mice were randomly allocated into five groups (G1–G5, $n = 3$ mice for each group). After being treated for 12 d, the CT26 cells were i.v. injected into these mice. On day 25, the mice were all sacrificed to collect the lungs for H&E staining assays.

In vivo anti-tumor immunity

For the macrophage polarization analysis, the tumors of mice with different treatments were extracted, homogenized in PBS, and filtered to obtain single-cell suspension. Subsequently, the cells were stained with anti-CD45-APC/Cyanine7, anti-CD11b-FITC, anti-F4/80-PerCP/Cyanine5.5, anti-CD86-APC, and anti-CD206-PE antibodies, and the macrophage phenotype was analyzed by flow cytometry.

For T-cell activation analysis, the collected spleens and tumors were homogenized in PBS, and filtered to obtain single-cell suspension. Afterwards, the cells were stained with anti-CD45-APC/Cyanine7, anti-CD3-PerCP/Cyanine5.5, anti-CD4-FITC, and anti-CD8a-APC, and the activation of T cells was analyzed by flow cytometry. The activated CD8 T cells were further analyzed by staining primary and distant tumor cells with anti-IFN-γ-PE antibodies.

For DCs maturation analysis, the collected spleens were homogenized in PBS, and filtered to obtain single-cell suspension. Afterwards, the cells were stained with anti-CD11c-FITC, anti-CD86-APC, and anti-CD80-PE antibodies to analyze the maturation of DCs using flow cytometry.

To analyze memory T cells, the collected spleens were homogenized in PBS, and filtered to obtain single-cell suspension. Afterwards, the cells were stained with anti-CD45-APC/Cyanine7, anti-CD3-PerCP/Cyanine5.5, anti-CD8a-APC, anti-CD44-FITC, anti-CD62L-PE antibodies to evaluate the memory T cell using flow cytometry.

RNA sequencing

The tumor-bearing mice were randomly allocated into two groups, including control and Pd_2Sn@GOx-SP + laser. After 1 week of treatment, the mice were sacrificed and the tumors were extracted for RNA sequencing according to the requirement of GENEWIZ, Inc. (Suzhou, China).

Statistical analysis

Quantitative data were indicated as mean ± S.D. The software of GraphPad Prism 9.0 was adopted to assess the statistical analysis, which was performed using the Student's t-test and one/two-way ANOVA. The statistical significance was attained at $^*p < 0.05$, $^{**}p < 0.01$, $^{***}p < 0.001$, and $^{****}p < 0.0001$.

Reporting summary

Further information on research design is available in the Nature Portfolio Reporting Summary linked to this article.

Data availability

The RNA-seq data generated in this study are available in the GSA database under accession code CRA016541 and could be achieved by the following hyperlink [https://ngdc.cncb.ac.cn/gsa/browse/CRA016541]. The remaining data generated in this study are available within the Article, Supplementary Information, or Source Data file. Source data are provided with this paper.

References

1. Siegel, R. L., Giaquinto, A. N. & Jemal, A. Cancer statistics, 2024. *CA Cancer J. Clin.* **74**, 12–49 (2024).
2. Dizon, D. S. & Kamal, A. H. Cancer statistics 2024: all hands on deck. *CA Cancer J. Clin.* **74**, 8–9 (2024).
3. Santucci, C. et al. European cancer mortality predictions for the year 2024 with focus on colorectal cancer. *Ann. Oncol.* **35**, 308–316 (2024).
4. Zhang, W., Hu, X., Shen, Q. & Xing, D. Mitochondria-specific drug release and reactive oxygen species burst induced by polyprodrug nanoreactors can enhance chemotherapy. *Nat. Commun.* **10**, 1704 (2019).
5. Malla, J. A. et al. A glutathione activatable ion channel induces apoptosis in cancer cells by depleting intracellular glutathione levels. *Angew. Chem. Int. Ed.* **59**, 7944–7952 (2020).
6. Machesky, L. M. Deadly actin collapse by disulfidptosis. *Nat. Cell Biol.* **25**, 375–376 (2023).
7. Liu, X., Zhuang, L. & Gan, B. Disulfidptosis: disulfide stress-induced cell death. *Trends Cell Biol.* **34**, 327–337 (2023).
8. Liu, X. et al. Cystine transporter regulation of pentose phosphate pathway dependency and disulfide stress exposes a targetable metabolic vulnerability in cancer. *Nat. Cell Biol.* **22**, 476–486 (2020).
9. Liu, X. et al. Actin cytoskeleton vulnerability to disulfide stress mediates disulfidptosis. *Nat. Cell Biol.* **25**, 404–414 (2023).
10. Koppula, P., Zhuang, L. & Gan, B. Cystine transporter SLC7A11/xCT in cancer: ferroptosis, nutrient dependency, and cancer therapy. *Protein Cell* **12**, 599–620 (2020).
11. Yan, Y. et al. SLC7A11 expression level dictates differential responses to oxidative stress in cancer cells. *Nat. Commun.* **14**, 3673 (2023).
12. Feng, Q. et al. Severely polarized extracellular acidity around tumour cells. *Nat. Biomed. Eng.* **2157**, 1–13 (2024).
13. Lin, F., Li, M., Zeng, L., Luo, M. & Guo, S. Intermetallic nanocrystals for fuel-cells-based electrocatalysis. *Chem. Rev.* **123**, 12507–12593 (2023).
14. Zhou, M., Li, C. & Fang, J. Noble-metal based random alloy and intermetallic nanocrystals: syntheses and applications. *Chem. Rev.* **121**, 736–795 (2021).
15. Yan, Y. et al. Intermetallic nanocrystals: syntheses and catalytic applications. *Adv. Mater.* **29**, 1605997 (2017).
16. Cui, Z. et al. Synthesis of structurally ordered Pt_3Ti and Pt_3V nanoparticles as methanol oxidation catalysts. *J. Am. Chem. Soc.* **136**, 10206–10209 (2014).
17. Gamler, J. T. L., Ashberry, H. M., Skrabalak, S. E. & Koczkur, K. M. Random alloyed versus intermetallic nanoparticles: a comparison of electrocatalytic performance. *Adv. Mater.* **30**, 1801563 (2018).
18. Chou, N. H. & Schaak, R. E. Shape-controlled conversion of β-Sn nanocrystals into intermetallic M-Sn (M = Fe, Co, Ni, Pd) nanocrystals. *J. Am. Chem. Soc.* **129**, 7339–7345 (2007).
19. Zhu, P. et al. MnOOH-catalyzed autoxidation of glutathione for reactive oxygen species production and nanocatalytic tumor innate immunotherapy. *J. Am. Chem. Soc.* **145**, 5803–5815 (2023).
20. He, S. et al. A semiconducting iron-chelating nano-immunomodulator for specific and sensitized sono-metallo-immunotherapy of cancer. *Angew. Chem. Int. Ed.* **62**, e202310178 (2023).
21. Wang, W. et al. A self-adaptive pyroptosis inducer: optimizing the catalytic microenvironment of nanozymes by membrane-adhered microbe enables potent cancer immunotherapy. *Adv. Mater.* **36**, 2310063 (2024).
22. Xu, X. et al. Virus-like particle-induced cGAS-STING activation and AIM2 inflammasome-mediated pyroptosis for robust cancer immunotherapy. *Angew. Chem. Int. Ed.* **62**, e202303010 (2023).
23. Li, F. et al. mRNA lipid nanoparticle-mediated pyroptosis sensitizes immunologically cold tumors to checkpoint immunotherapy. *Nat. Commun.* **14**, 4223 (2023).
24. Niu, R. et al. Programmed targeting pyruvate metabolism therapy amplified single-atom nanozyme-activated pyroptosis for immunotherapy. *Adv. Mater.* **36**, 2312124 (2024).
25. Wang, Q. et al. A bioorthogonal system reveals antitumour immune function of pyroptosis. *Nature* **579**, 421–426 (2020).
26. Yu, B. et al. Platinum prodrug nanoparticles with COX-2 inhibition amplify pyroptosis for enhanced chemotherapy and immune activation of pancreatic cancer. *Adv. Mater.* **36**, 2310456 (2024).
27. Zhao, Q. et al. Dual active centers linked by a reversible electron station as a multifunctional nanozyme to induce synergetically enhanced cascade catalysis for tumor-specific therapy. *J. Am. Chem. Soc.* **145**, 12586 (2023).
28. Lin, H., Wang, Y., Gao, S., Chen, Y. & Shi, J. Theranostic 2D tantalum carbide (MXene). *Adv. Mater.* **30**, 1703284 (2018).
29. Liu, P. et al. Photochemical route for synthesizing atomically dispersed palladium catalysts. *Science* **352**, 797 (2016).
30. Huang, L. et al. Synergy between plasmonic and electrocatalytic activation of methanol oxidation on palladium-silver alloy nanotubes. *Angew. Chem. Int. Ed.* **58**, 8794–8798 (2019).
31. Li, S. et al. Degradable holey palladium nanosheets with highly active 1D nanoholes for synergetic phototherapy of hypoxic tumors. *J. Am. Chem. Soc.* **142**, 5649–5656 (2020).
32. Li, S. et al. Tensile-strained palladium nanosheets for synthetic catalytic therapy and phototherapy. *Adv. Mater.* **34**, 2202609 (2022).
33. Fu, Q., Zhu, R., Song, J., Yang, H. & Chen, X. Photoacoustic imaging: contrast agents and their biomedical applications. *Adv. Mater.* **31**, 1805875 (2019).
34. Lin, L. & Wang, L. V. The emerging role of photoacoustic imaging in clinical oncology. *Nat. Rev. Clin. Oncol.* **19**, 365–384 (2022).
35. Jia, X., Wang, J. & Wang, E. Rapid synthesis of trimetallic nanozyme for sustainable cascaded catalytic therapy via tumor microenvironment remodulation. *Adv. Mater.* **36**, 2309261 (2024).
36. Wang, Z. et al. 2D catalytic nanozyme enables cascade enzyodynamic effect-boosted and Ca^{2+} overload-induced synergistic ferroptosis/apoptosis in tumor. *Adv. Mater.* **36**, 2312316 (2024).
37. Xu, J. et al. Carbon dioxide electroreduction into syngas boosted by a partially delocalized charge in molybdenum sulfide selenide alloy monolayers. *Angew. Chem. Int. Ed.* **56**, 9121–9125 (2017).
38. Sousa de Almeida, M. et al. Understanding nanoparticle endocytosis to improve targeting strategies in nanomedicine. *Chem. Soc. Rev.* **50**, 5397–5434 (2021).
39. Donahue, N. D., Acar, H. & Wilhelm, S. Concepts of nanoparticle cellular uptake, intracellular trafficking, and kinetics in nanomedicine. *Adv. Drug Deliv. Rev.* **143**, 68–96 (2019).
40. Wang, Y.-F. et al. Spatiotemporal tracing of the cellular internalization process of rod-shaped nanostructures. *ACS Nano* **16**, 4059–4071 (2022).
41. Rennick, J. J., Johnston, A. P. R. & Parton, R. G. Key principles and methods for studying the endocytosis of biological and nanoparticle therapeutics. *Nat. Nanotechnol.* **16**, 266–276 (2021).

42. Yao, C. et al. Near-infrared upconversion mesoporous cerium oxide hollow biophotocatalyst for concurrent pH-/H_2O_2-responsive O_2-evolving synergetic cancer therapy. *Adv. Mater.* **30**, 1704833 (2018).
43. Yu, P. et al. Pyroptosis: mechanisms and diseases. *Signal Transduct. Target. Ther.* **6**, 128 (2021).
44. Zhang, L. et al. Integration of AIEgens into covalent organic frameworks for pyroptosis and ferroptosis primed cancer immunotherapy. *Nat. Commun.* **14**, 5355 (2023).
45. Kalyane, D. et al. Reactive oxygen nano-generators for cancer therapy. *Prog. Mater. Sci.* **130**, 100974 (2022).
46. Chang, M. et al. Ultrasound-amplified enzyodynamic tumor therapy by perovskite nanoenzyme-enabled cell pyroptosis and cascade catalysis. *Adv. Mater.* **35**, 2208817 (2023).
47. Yang, Y. et al. Electrostatic attractive self-delivery of siRNA and light-induced self-escape for synergistic gene therapy. *Adv. Mater.* **35**, 2301409 (2023).
48. Xu, K. et al. Multienzyme-mimicking $LaCoO_3$ nanotrigger for programming cancer-cell pyroptosis. *Adv. Mater.* **35**, 2302961 (2023).
49. Zhang, S. et al. Biomineralized two-enzyme nanoparticles regulate tumor glycometabolism inducing tumor cell pyroptosis and robust antitumor immunotherapy. *Adv. Mater.* **34**, 2206851 (2022).
50. Aboushousha, R. et al. Glutaredoxin attenuates glutathione levels *via* deglutathionylation of Otub1 and subsequent destabilization of system x_C^-. *Sci. Adv.* **9**, eadi5192 (2023).
51. Zhao, X. et al. Orchestrated yolk–shell nanohybrids regulate macrophage polarization and dendritic cell maturation for oncotherapy with augmented antitumor immunity. *Adv. Mater.* **34**, 2108263 (2022).
52. Palucka, K. & Banchereau, J. Cancer immunotherapy *via* dendritic cells. *Nat. Rev. Cancer* **12**, 265–277 (2012).
53. Liu, Y. et al. Chemical design of activatable photoacoustic probes for precise biomedical applications. *Chem. Rev.* **122**, 6850–6918 (2022).
54. Lee, N., Choi, S. H. & Hyeon, T. Nano-sized CT contrast agents. *Adv. Mater.* **25**, 2641–2660 (2013).
55. Zhang, L. et al. Engineering multienzyme-mimicking covalent organic frameworks as pyroptosis inducers for boosting antitumor immunity. *Adv. Mater.* **34**, 2108174 (2022).
56. Hoekstra, M. E. et al. Long-distance modulation of bystander tumor cells by $CD8^+$ T-cell-secreted IFN-γ. *Nat. Cancer* **1**, 291–301 (2020).
57. Sylvestre, M., Crane, C. A. & Pun, S. H. Progress on modulating tumor-associated macrophages with biomaterials. *Adv. Mater.* **32**, 1902007 (2020).
58. DeNardo, D. G. & Ruffell, B. Macrophages as regulators of tumour immunity and immunotherapy. *Nat. Rev. Immunol.* **19**, 369–382 (2019).
59. Chen, S. et al. Macrophages in immunoregulation and therapeutics. *Signal Transduct. Target. Ther.* **8**, 207 (2023).
60. Xia, Y. et al. Engineering macrophages for cancer immunotherapy and drug delivery. *Adv. Mater.* **32**, 2002054 (2020).
61. Ovais, M., Guo, M. & Chen, C. Tailoring nanomaterials for targeting tumor-associated macrophages. *Adv. Mater.* **31**, 1808303 (2019).
62. Zhang, X. et al. Reprogramming tumour-associated macrophages to outcompete cancer cells. *Nature* **619**, 616–623 (2023).
63. Guo, Y., Hu, P. & Shi, J. Nanomedicine remodels tumor microenvironment for solid tumor immunotherapy. *J. Am. Chem. Soc.* **146**, 10217–10233 (2024).

Acknowledgements

Financial support from the National Natural Science Foundation of China (NSFC 52002091 to L.F., U22A20347 to P.Y., and U22A20316 to Y. Zhou), Heilongjiang Natural Science Foundation Project of Outstanding Youth Project (YQ2023B005 to L.F.), Natural Science Foundation of Heilongjiang Provincial Government (LH2022H067 to B.L.), China Postdoctoral Science Foundation (2023TQ0091 to L.F.), Heilongjiang Postdoctoral Fund (LBH-Z23014 to B.L.), Ph.D. Student Research and Innovation Fund of the Fundamental Research Funds for the Central Universities (3072023GIP1002 to Y. Zhu), and the Fundamental Research Funds for the Central Universities. The authors would like to thank Ruifang Shen from Harbin Institute of Technology, Institute of Space Environment and Materials Science (National Major Science Engineering) for CT and PA imaging tests.

Author contributions

These authors contributed equally: Y. Zhu and X. Wang. Y. Zhu and X.W. conceived the idea and designed the project. Y. Zhu, X.W., R.Z., and C.Y. performed the experiments and analyzed the results. L.F., Y.L., B.L., and Y. Zhou assisted with the experiment design and data analysis. Y. Zhu wrote and revised the original draft of the manuscript. Y.X. performed the DFT calculations. L.F., Y.X., and Y. Zhou reviewed and edited the manuscript. P.Y. supervised the whole project. All authors discussed the results and commented on the manuscript.

Competing interests

The authors declare no competing interests.

Additional information

Supplementary information The online version contains supplementary material available at https://doi.org/10.1038/s41467-024-53135-2.

Correspondence and requests for materials should be addressed to Lili Feng, Yang Zhou or Piaoping Yang.

Peer review information *Nature Communications* thanks Jie Han, Kohsuke Tsuchiya, XueBo Yin, and the other, anonymous, reviewer(s) for their contribution to the peer review of this work. A peer review file is available.